Li et al. *Microsystems & Nanoengineering* (2026)12:191
https://doi.org/10.1038/s41378-026-01325-x

Microsystems & Nanoengineering
www.nature.com/micronano

ARTICLE Open Access

A robotic patch-clamp system with real-time localization and phase-synchronized capture of dynamic in vivo cells using micropipette resistance modelling

Ruimin Li[1,2], Hao Chen[1,2], Bo Hu[1,2], Jinyu Qiu[1,2], Yuzhu Liu[1,2], Zijian Guo[1,2], Shouguo Wu[1,2], Mengya Liu[1,2], Ran Ding[3], Shengkai Ding[4], Yuanyuan Li[4], Xiaogang Pang[5], Hui Shen[6], Qili Zhao[1,2,7] and Xin Zhao[1,2]

Abstract

In vivo patch clamp is the gold standard for probing neuronal function in the intact brain of living animals through recordings of membrane potentials and picoampere-level ionic currents. To achieve this, the recording micropipette must first capture a target neuron and form a gigaohm-scale seal (gigaseal) at the cell membrane. This requires real-time localization of in vivo neurons whose positions fluctuate with physiological activity (e.g., respiration and vascular pulsation). Although two-photon microscopy enables cellular visualization, real-time motion tracking is constrained by the trade-off between imaging depth and temporal resolution, compromising capture success for moving cells. Here, we present a real-time localization method that enables vision-independent tracking of single-cell motion using micropipette resistance modeling. To denoise resistance signals, we develop a Multiple-Dominant-Frequency Weighted-Frequency Fourier Linear Combiner-Kalman Filter, enabling the tracking of neuronal motion with an average estimation error below 0.5 μm. We further introduce a phase-synchronized capture strategy that advances the micropipette to capture the in vivo cell at the farthest position in its motion cycle, thereby facilitating gigaseal formation. Based on the above work, we establish a robotic in vivo patch-clamp system that achieves an 81.8% gigaseal success rate in anesthetized mice, exceeding previously reported rates (~51% and ~24%) for robotic blind patch-clamp systems. We additionally obtain in vivo patch-clamp recordings in anesthetized rats and in both anesthetized and awake marmosets, representing the first demonstration of robotic in vivo patch-clamp recordings in awake marmosets and highlighting the robustness of our system across species and brain states.

Introduction

In vivo patch-clamp is a gold-standard technique for probing neuronal function in the intact brain of living animals through direct measurements of membrane potentials and picoampere-level ionic currents[1–5]. The in vivo patch clamp technique is schematically shown in Fig. 1a. The operator usually uses a glass micropipette with a micron-sized opening, which is filled with conductive solution and inserted with an electrode wire to form a micropipette electrode, to contact the membrane of an in vivo neuron in the animal brain. Gentle negative pressure is then applied to aspirate a small patch of membrane into the micropipette opening, forming a gigaseal between the inner wall of the micropipette and the aspirated membrane. This gigaseal can effectively isolate the recording from environmental electrical noise, enabling measurements of picoampere-level (10^{-12} A) ionic currents flowing through ion channels in the neuronal membrane.

Correspondence: Qili Zhao (zhaoqili@nankai.edu.cn) or
Xin Zhao (zhaoxin@nankai.edu.cn)
[1]National Key Laboratory of Intelligent Tracking and Forecasting for Infectious Diseases, Engineering Research Center of Trusted Behavior Intelligence, Ministry of Education, Tianjin Key Laboratory of Intelligent Robotics, Institute of Robotics and Automatic Information System, Nankai University, Tianjin, China
[2]Institute of Intelligence Technology and Robotic Systems, Shenzhen Research Institute of Nankai University, Shenzhen, China
Full list of author information is available at the end of the article

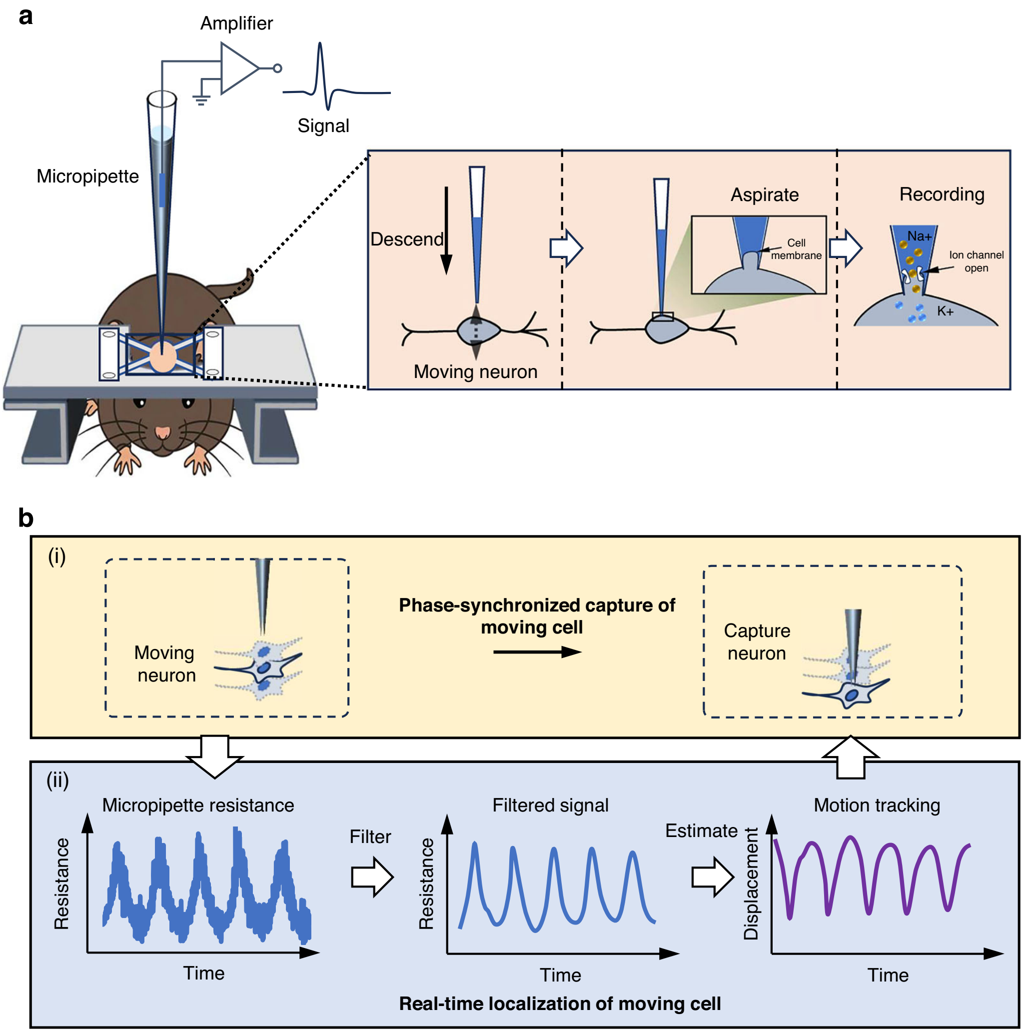

Fig. 1 Schematic of cell localization and capture. a In vivo patch-clamp workflow. The micropipette is advanced toward a moving neuron. Upon contacting the neuronal membrane, negative pressure is applied to aspirate a membrane patch and form a gigaseal, a prerequisite for high-quality in vivo patch-clamp recordings. **b** Schematic of micropipette resistance-based cell localization and capture. Localization is performed in two steps: (1) denoising the resistance signal using the MDF-WFLC-KF and (2) converting the filtered resistance into an accurate proximity estimate using the proposed resistance-distance model. Cell capture is achieved by synchronizing the micropipette tip arrival with the cell's farthest position in its motion cycle

As mentioned above, forming a gigaseal requires the micropipette tip opening to precisely capture the target neuron. This task faces significant challenges due to the complex in vivo operating environment. Intrinsic physiological processes in living animals, such as respiration and cardiac pulsation, induce substantial quasi-periodic motion, causing target cells to move dynamically. These motion-induced drifts make it extremely challenging to precisely capture a moving cell to initiate gigaseal formation.

A common practice is to mitigate in vivo cell motion to increase the success rate of precisely capturing a cell for gigaseal formation. Multiple immobilization devices have been developed to stabilize specific parts of the animal. For example, rigid head-fixation systems have been developed to reduce brain motion by immobilizing the cranium[6,7]. However, residual neuronal motion persists due to the compliant nature of the skull and its non-rigid coupling with the underlying brain tissue, which interferes with high-precision neuron capture. Another common strategy to reduce environmental displacement is to minimize the size of craniotomy (typically less than 1 mm in diameter in mice), preserving as much mechanical constraint from the cranium as possible[8,9]. However, this approach severely restricts the workspace and limits micropipette maneuverability, particularly in multi-micropipette or deep-brain applications.

Beyond passive stabilization, physiology-driven synchronization has been explored to improve the efficiency of capturing dynamically moving cells in vivo. A previous study[10] utilized physiological signals, including electrocardiogram (ECG), respiratory pressure, and cranial displacement, to estimate brain motion trajectories and synchronize micropipette movements, thereby creating a relatively stable manipulation environment and reducing relative brain motion-induced artifacts. However, this approach has two key limitations. First, mechanical decoupling exists not only between the skull and the brain but also between global brain motion and the localized displacement of individual neurons. As a result, residual relative motion between the micropipette tip and the target membrane can persist even after synchronization. Second, it relies on complex instrumentation, such as laser interferometers to measure cranial motion and pressure sensors for respiration monitoring, increasing system complexity and technical overhead, which may hinder broader adoption in routine in vivo patch-clamp experiments.

Another effective way to improve the efficiency of capturing neurons in the living brain is to perform real-time, accurate dynamic localization of target cells. Recent advances in imaging technologies for biological tissues, particularly two-photon microscopy, enable direct visualization of labeled neurons and their lateral motion in vivo[11,12], as well as indirect localization of unlabeled neurons via shadow imaging using fluorescent dye delivered from the recording micropipette[13,14]. Leveraging these capabilities, targeted patch-clamp recordings[15] have been demonstrated by iteratively adjusting micropipette position toward target neurons in the living brain. However, this approach has several important limitations. First, volumetric two-photon imaging relies on sequential scanning and can be too slow to track fast in vivo dynamics. For example, forming a 512 × 512 × 20 voxel stack typically requires ~0.6 s using a 30 Hz resonant scanner[16], which is insufficient to track heartbeat-driven displacement (~6 Hz) with peak-to-peak amplitudes of up to ~10 μm in anesthetized mice[17,18], especially along the depth (Z) axis. In addition, although imaging depths approaching ~1 mm are possible under favorable conditions, the effective imaging depth is often <500 μm in practice due to tissue scattering[5]. This limitation severely restricts its applicability for targeting neurons in deeper brain regions, such as the hippocampal CA3, thalamus, and other subcortical nuclei. Additionally, integrating two-photon imaging into patch-clamp manipulation setups substantially increases experimental complexity and cost (often several hundred thousand USD), creating a barrier to routine use.

Blind in vivo patch-clamp uses changes in micropipette resistance, rather than microscopic visual feedback, to sense neuronal proximity[5,19]. Because the neuronal membrane is much less conductive than the extracellular fluid, micropipette resistance increases significantly as the tip approaches the neuronal surface due to the reduced volume of conductive fluid between them. Existing approaches usually rely on an empirical rise in resistance as a qualitative indicator of proximity[5,19,20]. However, in the absence of a quantitative resistance-distance model, such empirical cues cannot estimate the actual tip-to-membrane distance and therefore cannot reliably regulate the final micrometers of approach required for stable contact and gigaseal formation. More recently, one study[18] leveraged resistance information to guide micropipette navigation in vivo but did not explicitly estimate the tip-membrane distance. Instead, proximity was inferred indirectly by iteratively minimizing resistance fluctuations. Without real-time quantitative distance feedback, the micropipette may retract prematurely or accidentally penetrate the membrane, leading to unstable or failed recordings. Overall, for dynamically moving neurons in vivo, blind navigation during the critical final approach remains weakly informed and often trial-and-error, reducing yield and limiting throughput.

To address these limitations, we developed a vision-independent, micropipette resistance-based localization method that estimates the distance between the micropipette tip and the neuronal membrane in real time during in vivo manipulation. To reduce environmental noise, we introduce a novel filtering algorithm, the Multiple Dominant Frequency Weighted-Frequency Fourier Linear Combiner Kalman Filter (MDF-WFLC-KF), which preserves the phase of motion-induced signals while minimizing latency in resistance measurements. Building on this localization capability, we further propose a phase-synchronized capture strategy for dynamically moving cells that advances the micropipette tip to contact the membrane at the cell's farthest excursion within its motion cycle. By integrating the real-time localization with this capture strategy, we establish a robotic patch-clamp framework that estimates the tip-membrane distance and captures cells to facilitate in vivo gigaseal formation, as shown in Fig. 1b.

To validate the performance of the proposed filtering method, we conducted comparative experiments on in vivo micropipette resistance recordings using two filtering algorithms (MDF-WFLC and EKF). The results show that our method achieves superior signal fidelity, with the lowest RMSE of 13.085 ± 1.86 pA, the highest signal-to-noise ratio of 59.07 ± 3.192 dB, and a computational latency of ~0.056 ms per sample. These findings confirm its capability for real-time noise suppression, laying the foundation for precise proximity estimation between the micropipette tip and the cell membrane. To further assess the accuracy of dynamic motion measurement, the micropipette was driven to perform periodic motions in acute brain slices to mimic in vivo relative neuronal displacement. The estimated proximity values exhibited errors of less than 0.5 μm, demonstrating high localization precision. Based on this localization capability, we developed a phase-synchronized capture strategy that synchronizes micropipette tip arrival with the cell's farthest position (FP) within its motion cycle. The final seal resistance at FP was the highest, reaching up to 55-fold higher than that obtained using other strategies. Finally, we integrated the proposed localization method and capture strategy into an in vivo patch-clamp manipulation platform to enable robotic in vivo patch-clamp operation. Both cell-attached and whole-cell recordings using this system showed a significant improvement in gigaseal formation success rate compared with previous robotic systems, demonstrating the robustness of our framework under dynamic physiological conditions. We further extended the robotic system to rats and to marmosets, obtaining in vivo patch-clamp recordings in anesthetized rats and in both anesthetized and awake marmosets. Notably, these results represent the first demonstration of robotic in vivo patch-clamp recordings in awake non-human primates (marmosets), highlighting robust performance across species and brain states.

Methods and materials

System setup for in vivo single-cell dynamic motion measurement

The developed in vivo cell dynamic motion measurement system consists of the following three modules: a supporting platform module, a manipulation module, and a signal measurement module, as shown in Fig. 2a. The supporting platform module consists of a commercial pneumatically active vibration isolation table (63-7512 M, TMC, Peabody, MA, USA), which provides a stable and level working surface, and a custom-designed mouse head-fixation device for skull immobilization. The fixation device includes a support stage and a head bar, as shown in Fig. 2a. The head bar is attached to the animal's skull with dental cement and subsequently secured to the support stage (Fig. 2b). A photograph of the actual system picture is provided in Fig. S1 of the Supplementary Information.

Regarding the manipulation module, a motorized manipulator (S-PS-7000C, Scientifica, Uckfield, UK) was used to precisely control micropipette motion, with a travel range of 20 mm × 20 mm ×20 mm and a resolution of 20 nm. The micropipettes used in this work were fabricated from commercial borosilicate glass capillaries (BF150-86-10, Sutter Instrument, Novato, CA, USA) with an outer diameter of 1.5 mm and an inner diameter of 0.86 mm using a commercial micropipette puller (P-97, Sutter Instrument, Novato, CA, USA). The pull program used in this study was set as follows: heat = 540, pull = 0, velocity = 30, and time = 250. It should be noted that these parameters are dimensionless, instrument-specific settings rather than physical quantities with SI units. Before being pulled by the P-97 puller, the borosilicate glass capillary was bent by 30° from its original axis using an alcohol burner, so that after mounting on the manipulator, the micropipette tip was approximately vertical relative to the horizontal plane (Fig. 2b(iii)).

As for the signal measurement module, a commercial patch-clamp system was employed for both micropipette resistance measurement and neuronal electrophysiological recordings. An amplifier (MultiClamp 700B, Molecular Devices, San Jose, CA, USA), together with a digital-to-analog converter (Digidata 1550B, Molecular Devices, San Jose, CA, USA), was used to measure the micropipette current at the picoampere (pA) level because of the small opening of the micropipette tip. However, because the data acquisition and processing functions of this commercial system are highly encapsulated within proprietary software, it is difficult to access raw electrophysiological signals in real time for customized analysis. To overcome this limitation, we developed an independent data acquisition system (DAQS) capable of capturing the amplifier's analog output signals and converting them into digital form using a high-precision data acquisition card (NI USB 6211, National Instruments, Austin, TX, USA). These digitized signals were then transmitted to the host computer, enabling real-time monitoring, visualization, and processing. This system allows flexible integration of our custom algorithms for signal filtering and tip-membrane proximity sensing, thereby providing a more adaptable and extensible experimental platform. The system was also integrated with another data acquisition card (Smacq USB-3100, Smacq, Beijing, China) to achieve the precise injection pressure control. Pressure control is essential for patch-clamp manipulation, in which positive pressure helps prevent clogging at the micropipette tip, whereas negative pressure facilitates gigaseal formation between the tip and the cell membrane.

Based on the hardware described above, we developed host-computer software using the Qt framework to integrate hardware control and the proposed algorithms into a graphic user interface, as shown in Fig. 2c. The software communicates with all hardware components, including the micromanipulator, DAQS, and pressure sensor via USB connections. The DAQS acquires electrophysiological signals from the amplifier for real-time processing at sampling rates up to 20 kHz and regulates the electronic pressure controller using pressure-sensor feedback, achieving precise pressure control with a resolution of 10 Pa[21]. In addition, the proposed filtering algorithm, micropipette resistance model, and robotic patch-clamp workflow are integrated into the user

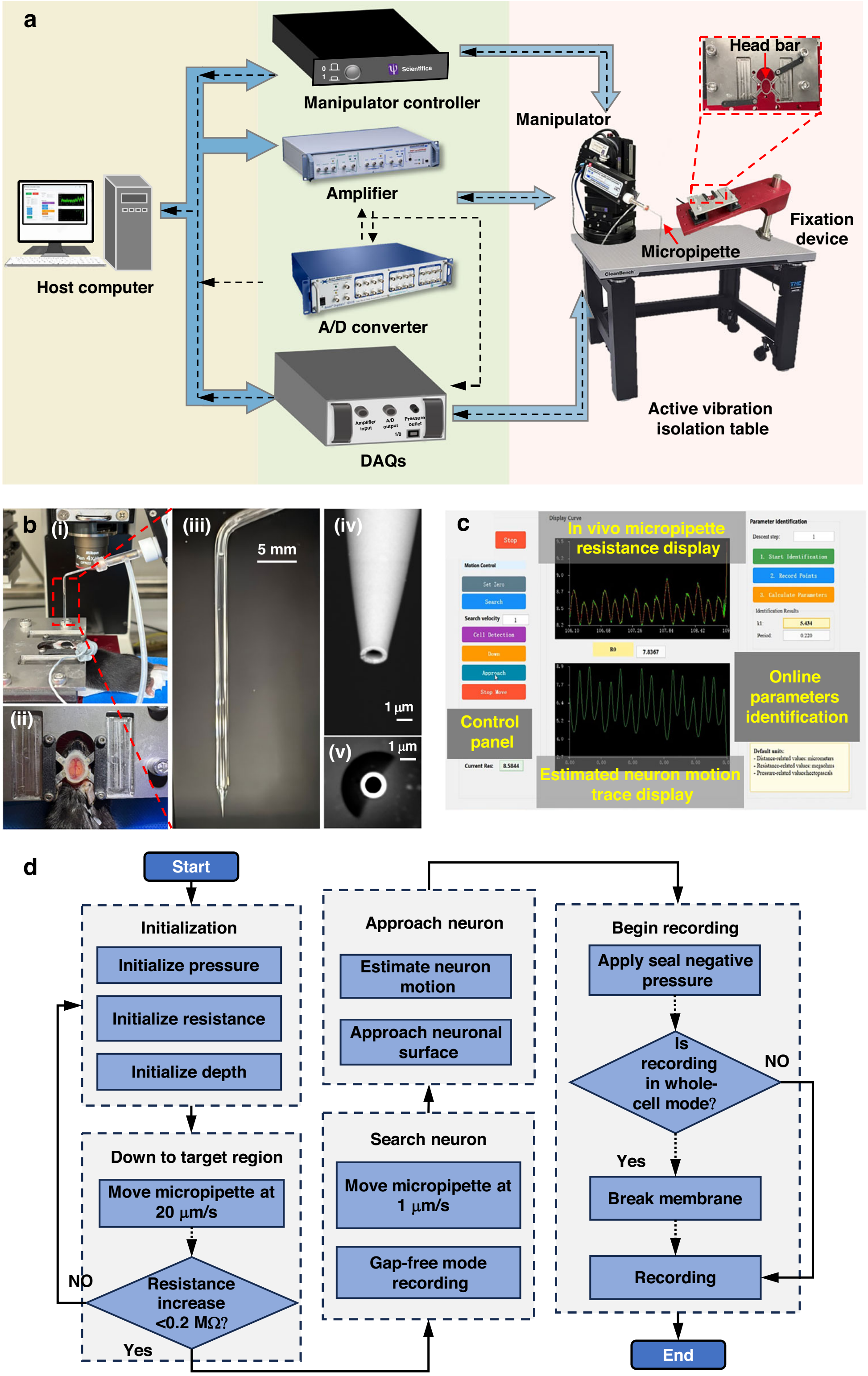

Fig. 2 System setup for in vivo patch-clamp recording. a Schematic diagram of the system hardware connections. Blue arrows represent control flow, while the black dashed arrows indicate data flow. **b** Photograph of in vivo patch-clamp recording in a mouse. (i) The mouse head is fixed on a custom-designed fixation device. (ii) Top view of Figure i. The mouse skull is attached to the head bar and secured to the fixation device with screws. (iii) Image of the customized micropipette. (iv) Side-view SEM image of the micropipette opening. (v) End-view SEM image of the micropipette opening. **c** Schematic of the self-developed UI interface for the in vivo manipulation system. **d** Flowchart of the robotic in vivo patch-clamp procedure

interface, allowing users to perform in vivo patch-clamp recording directly from the software. This software system simplifies in vivo cell operation and improves operational efficiency.

Micropipette resistance-based real-time localization of moving cells in vivo

Micropipette resistance modeling for distance estimation

The electrical resistance recorded from a micropipette originates from two primary sources: the resistance along the narrow micropipette interior and the resistance at the micropipette opening where ions exchange with the extracellular medium. Following the classical framework established in previous works[22,23], the overall micropipette resistance can therefore be expressed as the sum of the series resistance R_s and the access resistance R_a, as shown in Fig. 3a.

The series resistance R_s is determined by the micropipette geometry and can be expressed as follows:

$$R_s = \frac{\rho}{\pi \tan(\theta)} \left(\frac{1}{r_i} - \frac{1}{r_i + z\tan(\theta)} \right) \tag{1}$$

in which r_i is the inner opening radius, θ is the taper angle of the inner wall, z is the length of the micropipette cone, and ρ is the conductivity of the micropipette solution. In our experimental setup, $z \gg r_i$, and thus this expression can be approximated as follows:

$$R_s \approx \frac{\rho}{r_i \pi \tan(\theta)} \tag{2}$$

The detailed derivation is provided in Section 2 of the Supplementary Information.

The access resistance R_a describes the hindrance to ion flow at the micropipette opening. In a free solution, it is given by

$$R_a = \frac{\rho}{4r_i} \tag{3}$$

which is derived under the classical assumption that the micropipette tip faces an infinite, unbounded conductive half-face[24,25]. However, when the micropipette tip approaches a surface, and the tip-sample distance d becomes comparable to r_i, this half-space approximation breaks down. To account for these situations, previous studies[23,26] have modeled the gap between the micropipette tip and the sample as a concentric hollow cylinder filled with electrolyte, as shown in Fig. 3b. The inner radius corresponds to the micropipette tip radius, r_i, whereas the outer radius corresponds to the outer radius of the micropipette tip, r_o. Assuming that ionic current flows radially from the inner surface to the outer surface and is uniformly distributed along the cylinder height d (tip-sample distance), the differential resistance with respect to r is given by

$$dR = \frac{\rho dr}{2\pi r d} \tag{4}$$

Integration from $r = r_i$ to $r = r_i + d$ yields

$$R_a(d) = \frac{\rho}{2d\pi} \ln\left(\frac{\mathrm{r_o}}{\mathrm{r_i}} \right) \tag{5}$$

While these two limiting cases $(\mathrm{d} \to \infty andd \le r_i)$ provide useful theoretical insights, our experiments typically operate at intermediate tip-sample distances. In this range, the access resistance deviates from the ideal analytical expressions because of field-line curvature, where current flow is no longer perfectly radial near the tip, and because of the boundary conditions imposed by the nearby cell membrane, which alter the local potential and current distribution. To account for these non-ideal effects, we introduce a composite model in which dimensionless correction parameters, k_1, k_2, n are incorporated to capture field-line curvature, boundary-condition modifications, and nonlinear dependence on tip-cell distance, respectively. Accordingly, the distance-dependent access resistance R_a is expressed as:

$$R_a(d) = k_1 \frac{\rho}{2\pi d^n} \ln\left(\frac{\mathrm{r_o}}{\mathrm{r_i}} \right) + \mathrm{k}_2 \frac{\rho}{4\mathrm{r_i}} \tag{6}$$

The parameters k_1, k_2, n will be calibrated by finite element modeling (FEM). When the micropipette opening approaches the cell membrane, additional deformation introduces an extra displacement, Δd [27], which depends on the injection pressure P, membrane Young's modulus E, and the tip-membrane distance d. This relationship can be expressed as,

$$\Delta d = f(d, P, E) \tag{7}$$

and identified using FEM.

Combing the above terms, the total micropipette resistance as a function of tip-cell distance is expressed as follows,

$$R(d) = k_1 \frac{\rho}{2\pi (d + f(d, P, E))^n} \ln\left(\frac{\mathrm{r_o}}{\mathrm{r_i}} \right) + \mathrm{k}_2 \frac{\rho}{4\mathrm{r_i}} + \frac{\rho}{\mathrm{r_i} \pi \tan(\theta)} \tag{8}$$

With this theoretical relationship between the micropipette resistance and tip-membrane distance, the vertical proximity of the cell relative to the micropipette can be quantitatively estimated.

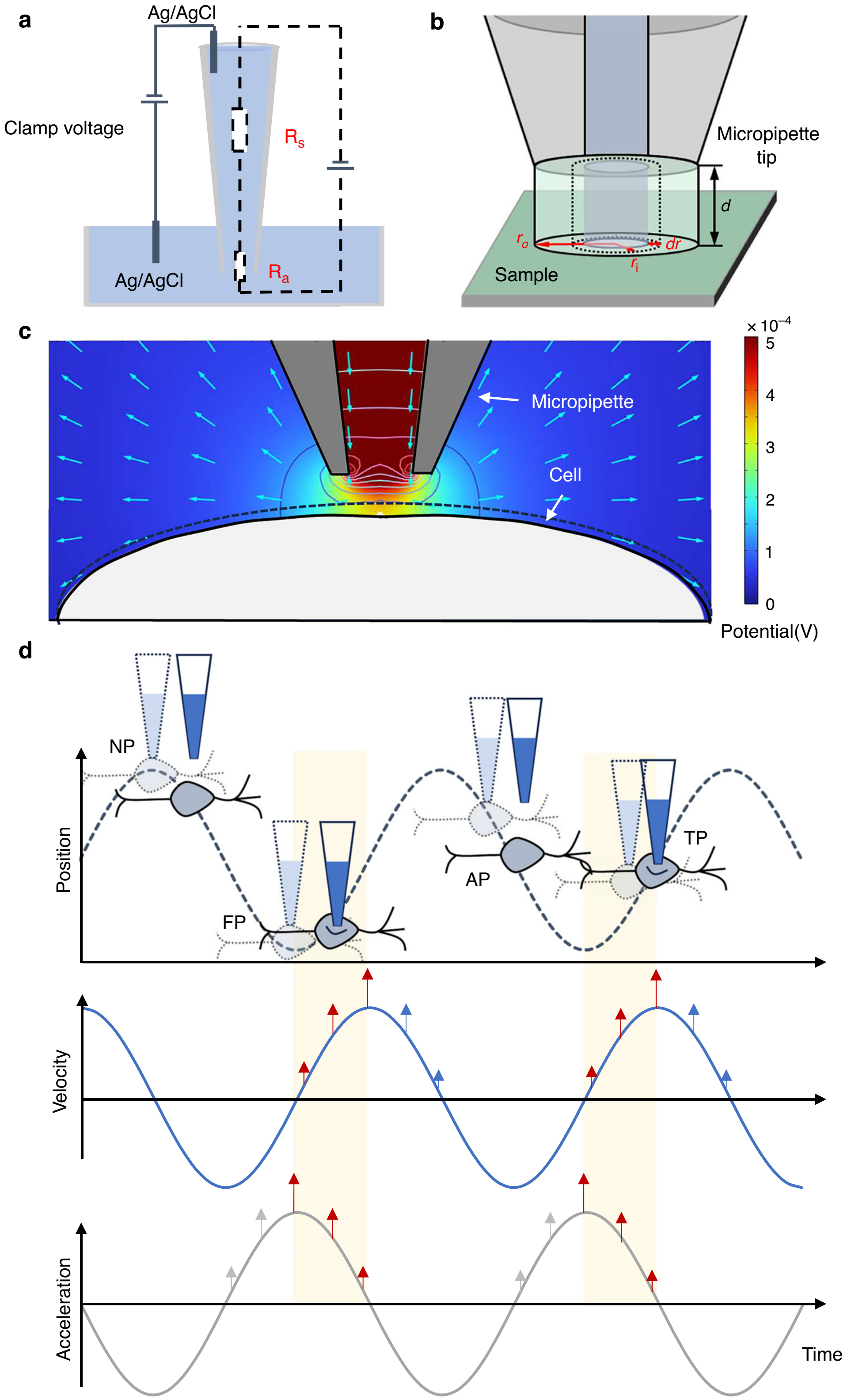

Fig. 3 (See legend on next page.)

(see figure on previous page)

Fig. 3 Schematic of the micropipette resistance-based localization method and the phase-synchronized capture strategy. a Equivalent circuit of the micropipette resistance, comprising the series resistance R_s and access resistance R_a. **b** Schematic of the theoretical derivation of R_a for the near-field regime $d \leq r_i$, where d is the tip-to-membrane distance and r_i is the inner radius of the micropipette tip. **c** Finite element simulation (FEM) showing cell deformation when the micropipette, under applied injection pressure, is positioned close to the cell. **d** Illustration of the four phase-synchronized capture strategies. Top: Four capture phases and their outcomes. The dashed sinusoidal curve indicates the neuron's motion trajectory. The dashed micropipette and cell illustrate their positions during execution of each strategy, whereas the solid micropipette and cell depict their relative configuration after completion of the strategy. After execution, the micropipette is held in a stable position while the cell continues its physiological motion. Middle: Corresponding velocity profile. Values above the horizontal axis indicate motion toward the micropipette; larger magnitudes indicate higher speed. Arrows denote the direction of motion, and longer arrows indicate greater velocity magnitude. Bottom: Corresponding acceleration profile. Values above the horizontal axis indicate acceleration toward the micropipette, reflecting tissue-driven forces that push the cell toward the pipette. Upward arrows denote pipette-directed acceleration. The time interval during which both velocity and acceleration are directed toward the micropipette (red arrows) is the most favorable for stable contact and gigaseal initiation

FEM-based calibration of the micropipette resistance model

The theoretical analysis in section "Micropipette resistance modeling for distance estimation" suggests that micropipette resistance increases as the micropipette tip approaches the cell surface. However, this process involves not only electrochemical effects but also fluid-solid coupling, making it difficult to determine certain unknown parameters analytically. To overcome this limitation, we employed FEM to simulate the micropipette-cell approach and to obtain a quantitative resistance-distance relationship for identifying these unknown parameters.

In this work, commercial FEM software (COMSOL Multiphysics) was employed to calculate changes in micropipette resistance during its approach toward the cell membrane. A geometric model of the micropipette tip was first constructed for this purpose. To obtain accurate geometric parameters, 15 micropipettes were imaged using scanning electron microscopy (SEM), and their tip morphologies were quantitatively analysed. The measurements showed that the average inner opening radius (r_i) was 0.56 ± 0.09 μm (mean ± SD, see Fig. S3), and the average outer opening radius (r_o) was 0.82 ± 0.26 μm (Fig. S3). In addition, the average cone angle (θ) was measured to be 2.93 ± 0.24° (Fig. S3) from microscopic images captured under a light microscope (Nikon, Japan). These experimentally obtained parameters were incorporated into the FEM model to ensure a realistic simulation of the micropipette resistance.

In the simulations, the micropipette was positioned at a vertical distance d from a deformable surface representing the cell, as shown in Fig. 3C. Neurons were simplified as flattened ellipsoids, with their surfaces modeled as electrical insulators. The cell body was treated as an elastic material, as the elastic response dominates the viscous response at the high frequencies[28]. The micropipette wall was also modeled as an insulating boundary. Full details of the model geometry and boundary conditions are provided in Section 4 of the Supplementary Information.

To extract the unknown coefficients k_1, k_2, and n, as well as the function f, the micropipette resistance was first obtained from FEM simulations. The series resistance (R_s) was calculated analytically using Eq. (1). The access resistance component, $R_a(d)$, was obtained as the difference between the FEM-calculated total resistance and the analytical expression for R_s. Subsequently, a least-squares fitting procedure was applied to fit $R_a(d)$ to the composite model, yielding calibrated values of k_1, k_2, and n, as well as the function f in Eq. (8). This calibration established an accurate functional relationship between micropipette resistance and tip-cell distance, enabling real-time estimation of the micropipette's proximity to the cell.

MDF-WFLC-KF for denoising of micropipette resistance signals

In addition to the need for an accurate resistance-distance model, environmental electrical noise poses another major challenge, as it contaminates the measured micropipette resistance and compromises the precise estimation of the tip-cell distance. Existing digital filter methods (Puce and Hämäläinen, 2017; Widmann et al., 2015) often introduce phase lag and amplitude distortion on the filtered signal, which are detrimental to accurately estimating the distance between the neuron membrane and the micropipette tip. The Kalman filter (Galleani and Tavella, 2010; Jacobs, 2020), known for preserving the phase and amplitude of the original signal, provides an optimal solution for linear system filtering. However, it is less suitable for estimating nonlinear components, such as frequency. Although the advanced variant, Unscented Kalman Filter (UKF) (Chow et al., 2007), has been developed to address nonlinearity, its computational complexity limits applicability in real-time tip-cell proximity estimation tasks. Adaptive methods, such as the Weighted Fourier Linear Combiner (WFLC) (Veluvolu and Ang, 2010), can adaptively track the frequency and amplitude of signals without introducing phase shift. However, WFLC is designed to track signals with a single dominant frequency. The recorded signals often exhibit two dominant frequency components (Zhang et al. [18]) induced by respiration and heartbeat, respectively, which limit the effectiveness of WFLC in such scenarios. Thus, an online filter method without phase lag and amplitude distortion is still desired.

To isolate these physiological frequency components from background noise while preserving their temporal characteristics, we developed a Multiple-Dominant-Frequency Weighted-Frequency Fourier Linear Combiner–Kalman Filter (MDF-WFLC-KF). The key idea is to separate frequency tracking from amplitude estimation: (1) two WFLC modules track the dominant frequencies and phase trajectories online; (2) given these phases, a linear Kalman filter estimates slowly varying Fourier coefficients for robust reconstruction.

Specifically, the measured resistance signal $r(k)$ is first passed through two causal 2nd-order Butterworth band-pass filters with cutoffs [0.5, 1.5] Hz and [3,8] Hz, corresponding to respiration- and heartbeat-related bands identified by FFT (approximately 1 Hz and 4 Hz). This band separation is used to improve SNR for frequency tracking; any fixed group delay introduced by the band-pass stage is treated as a constant delay and is compensated during signal alignment in the implementation so that the reconstructed motion component remains time-consistent with the raw measurements.

Let the two band-limited signals be $r_1(k)$ and $r_2(k)$. Each is processed by an independent WFLC to estimate the dominant frequency $\hat{f}_i(k)$ and its phase accumulator $\theta_i(k) (i \in \{1, 2\})$. Below, we present the WFLC formulation for $r_1(k)$; the same procedure applies to $r_2(k)$. We model the band-limited signal $r_1(k)$ as a truncated, time-varying Fourier series with M harmonics:

$$\hat{r}_1(k) = \sum_{m=1}^{M} [a_{1m}(k) \sin(m\theta_1(k)) + b_{1m}(k) \cos(m\theta_1(k))] \tag{9}$$

The phase accumulator evolves as

$$\theta_1(k) = \theta_1(k-1) + \omega_1(k) T_s,\ \omega_1(k) = 2\pi \hat{f}_1(k) \tag{10}$$

where T_s is the sampling period. Define the regressor and coefficient vector:

$$X_1(k) = [\sin(\theta_1(k)) \ldots\ \sin(M\theta_1(k)) \cos(\theta_1(k)) \ldots\ \cos(M\theta_1(k))]^T$$

$$W_1(k) = [a_{11}(k) \ldots\ a_{1M}(k)\, b_{11}(k) \ldots\ b_{1M}(k)]^T$$

respectively. The prediction and error are

$$\hat{r}_1(k) = W_1^T(k) X_1(k),\ e_1(k) = r_1(k) - \hat{r}_1(k) \tag{11}$$

Weights are updated by least mean square (LMS):

$$W_1(k+1) = W_1(k) + 2\mu_w X_1(k) e_1(k) \tag{12}$$

and the instantaneous angular frequency is updated by a gradient step:

$$\omega_1(k+1) = \omega_1(k) + \mu_\omega e_1(k) \frac{\partial \hat{r}_1(k)}{\partial \omega_1} \tag{13}$$

The explicit expression of $\partial \hat{r}_1(k) / \partial \omega_1$ follows from the chain rule through $\theta_1(k)$. In practice, μ_w, μ_ω, and M are selected to balance tracking responsiveness and noise robustness. The second WFLC operates identically on $r_2(k)$, producing $\hat{f}_2(k)$ and $\theta_2(k)$.

After obtaining $\hat{f}_i(k)$ and $\theta_i(k)$ from the two WFLCs, we construct a time-varying harmonic regressor using up to M harmonics per band:

$$X(k) = [\sin(\theta_1(k)), .., \sin(M\theta_1(k)), \cos\theta_1(k), .., \cos(M\theta_1(k)), \sin(\theta_2(k)), .., \sin(M\theta_2(k), \cos(\theta_2(k)), .., \cos M\theta_2(k)]^T \in \mathbb{R}^{4M\times 1} \tag{14}$$

The corresponding state vector stacks the Fourier coefficients of both bands:

$$W(k) = [a_{11}(k), .., a_{1M}(k), b_{11}(k), .., b_{1M}(k), a_{21}(k), .., a_{2M}(k), b_{21}(k), .., b_{2M}(k)]^T \in \mathbb{R}^{4M\times 1} \tag{15}$$

We model the motion-related resistance component $r(k)$ using a linear observation model:

$$r(k) = X^T(k) W(k) + \nu(k),\ \nu(k) \sim N(0, R) \tag{16}$$

Slow coefficient drift is captured by a random-walk state evolution:

$$W(k+1) = W(k) + q(k),\ q(k) \sim \mathrm{N}(0, Q) \tag{17}$$

Given $X(k)$ from WFLC phases trajectories, a standard linear Kalman filter estimates W(k) recursively:

Prediction

$$\hat{W}(k|k-1) = \hat{W}(k-1|k-1) \tag{18}$$

$$P(k|k-1) = P(k-1|k-1) + Q \tag{19}$$

Update

$$K(k) = P(k|k-1)X(k)\left(X^T(k)P(k|k-1)X(k) + R'\right)^{-1} \tag{20}$$

$$\hat{W}(k|k) = \hat{W}(k|k-1) + K(k)\left(r(k) - X^T(k)\hat{W}(k|k-1)\right) \tag{21}$$

$$P(k|k) = \left(I - K(k)X^T(k)\right)P_{k|k-1}P(k|k-1) \tag{22}$$

Finally, we get the filtered signal, expressed as follows,

$$\hat{r}(k) = X^T(k)\hat{W}(k|k) \tag{23}$$

In summary, the MDF-WFLC-KF first uses two WFLC trackers to obtain band-specific frequency and phase trajectories, which define a time-varying harmonic regressor. Treating the Fourier coefficients as a slowly varying linear state, a linear Kalman filter then provides robust, low-latency tracking of multi-frequency components in the presence of environmental noise. This split design avoids nonlinear Kalman filtering on frequency states, maintains real-time operation, and yields a phase-consistent reconstruction $\hat{r}_m(k)$ for subsequent tip-cell proximity estimation and motion-aware control. Since the heart- and respiration-related dominant frequencies evolve smoothly under relatively stable physiological conditions[29]. The filter-induced phase lag does not materially affect the estimated frequencies under our experimental conditions. Importantly, after the dominant frequencies are obtained, the subsequent MDF-WFLC-KF estimation is performed using the original (unfiltered) signal, rather than the band-pass-filtered signal. Therefore, the initial band-pass filtering does not introduce additional delay to the final MDF-WFLC-KF output. The workflow flowchart is shown in Fig. S5 of the Supplementary Information.

In implementation, the Fourier series order in Eq. (9) was set to $M = 2$ to balance waveform representation and computational cost for real-time operation. For the WFLC tracking of the lower dominant-frequency component (respiration band), the frequency adaptation factor was set to $\mu_\omega = 1\times10^{-4}$ and the weight adaptation factor to $\mu_w = 1\times10^{-6}$. For the higher dominant-frequency component (heartbeat band), $\mu_\omega = 5.1\times10^{-5}$ and $\mu_w = 5\times10^{-5}$ were used to provide faster coefficient adaptation while maintaining stable frequency tracking. In the Kalman filter stage, the process noise covariance was set to $Q = 1\times10^{-2}$ to allow slow drift of the Fourier coefficients, and the measurement noise covariance was set to $R = 63$ to account for residual disturbances in the resistance measurements. All computations were performed online at a sampling rate 1000 Hz.

Phase-synchronized capture strategy for moving cells in vivo

To achieve in vivo patch-clamp recordings under physiological motion, an appropriate phase-synchronized capture strategy is required in addition to accurate localization. We identify a favorable sealing window in the quasi-periodic cell motion, during which the cell moves toward the micropipette and exhibits micropipette-directed acceleration. We synchronize the micropipette tip–membrane contact to this window to maximize post-contact dwell time and reduce the likelihood of immediate separation, thereby increasing the probability of successful gigaseal initiation. In particular, the optimal capture phase occurs at the cell's farthest position (FP) relative to the micropipette tip, a turning point at which the instantaneous velocity is near zero, and the subsequent acceleration is directed toward the pipette, providing the longest continuous interval of motion toward the tip after contact. We selected three additional representative capture phases based on the estimated cell motion as baselines to assess whether FP is the optimal contact phase in living brain tissue. These phases are: NP, when the cell is nearest to the micropipette tip; AP, when the cell is moving away from the micropipette, and TP, when the cell is moving toward the micropipette tip.

Based on the estimated neuronal motion trajectories, the cell displacement relative to the micropipette tip is approximately sinusoidal. We therefore use an idealized sinusoidal model to interpret the qualitative differences among the four phase choices, as shown in Fig. 3d.

FP strategy

As illustrated in Fig. 3d, immediately after the FP turning point, the cell starts moving toward the micropipette (velocity directed toward the tip), and its acceleration is also directed toward the micropipette over an initial interval. This provides a sustained period of post-contact "active attachment," which reduces the likelihood of immediate separation and increases the available dwell time for gigaseal formation, thereby favoring higher seal resistance. Consistent with this analysis, FP yields the highest seal resistance in our experiments (experiment details in section "Results of phase-synchronized capture for dynamically moving cells in vivo").

TP strategy

The TP phase is similar in that the cell is already moving toward the micropipette at the moment of contact. However, compared with FP, the remaining duration of motion toward the micropipette after contact is shorter, resulting in a reduced attachment window. This suggests that TP should be less favorable than FP, which agrees with our experimental observation that FP produces higher seal resistance than TP.

NP strategy

For NP, contact occurs when the cell is at its nearest position to the micropipette. Immediately after this point, the cell motion reverses and begins to move away from the micropipette, with both velocity and acceleration directed away during the subsequent interval. As a result, the post-contact dwell time is minimal, and separation is likely, leading to poor gigaseal initiation and low seal resistance.

AP strategy

AP is related to NP in that contact occurs while the cell exhibits a tendency to move away from the pipette; however, in AP, the pipette "catches up" to the cell during the outgoing phase. This can provide slightly better conditions than NP, but because the cell continues to drift away after contact, AP is still expected to underperform TP and FP. Our experimental results (section "Results of phase-synchronized capture for dynamically moving cells in vivo") follow this trend: seal resistance under AP is higher than under NP, but lower than under TP and FP.

Robotic in vivo patch-clamp workflow

Figure 2d illustrates the workflow of the robotic in vivo patch-clamp process. By automating the essential procedures of in vivo patch-clamp, the system minimizes manual intervention while providing real-time tip–cell distance feedback and controlled micropipette advancement to the neuronal membrane, thereby improving the reliability of gigaseal formation.

Before the robotic operations begin, the micropipette is manually positioned above the cranial opening. The subsequent steps are then fully executed by the proposed system through a graphical user interface (GUI). During the initialization phase, a positive pressure of 40 hPa is automatically applied inside the micropipette to generate a fine outflow, thereby preventing clogging at the micropipette opening during searching for cells in the living brain. After 2 s, the system drives the micropipette to descend toward the cranial opening at a controlled speed of 0.5 μm/s. Once the micropipette tip contacts the tissue surface, an electrochemical conduction path forms between the micropipette interior and the extracellular environment. This transition from an open-circuit state to a conductive state enables resistance measurement. Under a constant holding voltage of -70 mV, a measurable current appears, and the corresponding apparent resistance drops to approximately 5-9 MΩ. At this moment, the descent of the micropipette is automatically paused. The measured resistance is recorded as the initial reference value R_0, and the corresponding vertical position is defined as the zero-depth level, serving as the baseline for determining the subsequent working depth.

During the descent to the region of interest, the micropipette is advanced along Z axis at a speed of 20 μm/s until reaching the target depth. At this point, the system automatically checks the micropipette resistance. If the resistance increases over 0.2 MΩ compared with the baseline resistance, the micropipette opening is considered clogged experimentally, in which case a new micropipette is required. After the micropipette is pulled out from the brain and replaced with a new one, the above procedures are repeated. Once the micropipette lowers down to the target depth, the system starts to search for the target cell.

During the target cell searching phase, the micropipette is advanced at a reduced speed of 1 μm/s to search for the target neuron. The system continuously records the current signal at a sampling rate of 20 kHz under a holding potential of -70 mV in gap-free mode, which allows uninterrupted measurements for several minutes. The micropipette resistance can be determined using Ohm's law. When the micropipette encounters a cell, the recorded resistance exhibits quasi-periodic fluctuations induced by cell motion, which originates from the intrinsic physiological activities such as heartbeat and respiration. Once the resistance fluctuation amplitude exceeds 0.3 MΩ, which is determined through large number of tests, and one of the dominant frequencies of the signal falls within 3 ~ 5 Hz, the micropipette motion is automatically halted, indicating that the micropipette tip is in the proximity of a cell. If no neuron is encountered during a given axial penetration attempt, the common practice is to retract the micropipette to the brain surface before performing a controlled lateral repositioning, followed by a new axial insertion for subsequent searching. Lateral exploration is not conducted within the brain tissue, but rather between discrete penetration attempts, in order to minimize cumulative tissue damage and reduce the likelihood of unintended collisions with surrounding structures.

During the approaching phase, the system first performs online calibration of the micropipette resistance-distance model. Because the theoretical model requires precise geometric parameters of the micropipette, which are time-consuming to measure for each experiment, an online parameter identification procedure is implemented. Specifically, the micropipette is driven to descend by a fixed step of <1 μm for at least three successive times, and the corresponding resistances after each step are recorded. The model coefficients are then estimated from these resistance-depth pairs using a least-squares fitting method. A detailed description of the online identification algorithm is provided in Section 5 of the Supplementary Information. After calibration, the system continuously filters the recorded current signals, which are often contaminated by environmental noise sing the proposed MDF-WFLC-KF algorithm. Based on the denoised signal and the identified model, the system estimates the relative distance between the micropipette tip and the cell membrane in real time. Following a 5 s observation period for motion estimation, the system implements the proposed phase-synchronized approaching strategy, advancing the micropipette so the tip reaches the cell membrane when the cell is at its farthest position relative to the tip within its motion cycle. Alternatively, the operator can manually select an appropriate time point to initiate the approaching procedure by clicking the corresponding button on the UI interface.

Immediately afterward, the injection pressure is switched to -40 hPa, and then maintained constant. When the micropipette resistance rises to the GΩ level and enters a stable state (lasting for more than 30 s), indicating the formation of a tight seal, the pressure is held steady for approximately 30 s to stabilize the attachment. Until now, the precise target operation has been achieved. After this, the user can select the desired recording mode by clicking the corresponding button, and the system initiates the appropriate signal acquisition.

Preparation of experimental samples

Mouse brain slice preparation

Adult C57BL/6 mice (6-8 weeks) are used in this work for validating the resistance-based distance sensing method. Mice are anesthetized via intraperitoneal injection of 1.25% Avertin (0.2 ml per 10 g body weight). Upon loss of reflexes, the head is quickly removed using surgical scissors, and the brain is immediately extracted and placed into ice-cold slicing solution (<3 °C) for further cooling. Coronal brain slices (300 μm thick) are prepared using a vibratome (7000smz-2, Campden Instruments, Loughborough, UK) in ice-cold slicing solution composed of (in mM): 110 choline chloride, 25 glucose, 7 $MgCl_2$, 2.5 KCl, 1.3 NaH_2PO_4, 0.5 $CaCl_2$, and 25 $NaHCO_3$, saturated with 95% O_2 and 5% CO_2. The slices are then transferred to a recovery chamber containing artificial cerebrospinal fluid (aCSF) at 37 °C for 40 minutes, followed by storage at room temperature (25 °C) until use. The aCSF used during recovery and recording has the same composition as the slicing solution.

Mouse craniotomy

Eight-week-old C57BL/6 mice are used in in vivo single-cell manipulation, including both whole-cell patch-clamp and cell-attached recordings. The mouse is first anesthetized using 1.25% Avertin (0.2 ml per 10 g body weight), and once reflexes are absent, the hair on the head is shaved using a razor. Ophthalmic ointment is applied to the eyes to prevent dryness and cataract formation. Body temperature is maintained at 37 °C using a homeothermic monitoring system (Harvard Apparatus, Holliston, MA, USA). The scalp is removed with surgical scissors to expose the skull. Residual fascia and periosteum are carefully removed to ensure proper adhesion between the skull and the dental cement. The head is then positioned in a stereotaxic frame (Narishige, Tokyo, Japan) and head is fixed by ear bars. Custom-built head bar (Fig. 2b(ii)) is adhered to the skull using dental cement. After the dental cement has cured, a craniotomy is performed using a precision drill equipped with a 0.3 mm diameter burr, resulting in an opening of approximately 3 mm in diameter. The dura mater is carefully removed with fine forceps to expose the brain surface, preventing damage to the underlying tissue. Removing the dura helps prevent the clogging of the micropipette tip during insertion. Once the brain surface is exposed, aCSF is applied to keep surface neurons viable. After surgery, the mouse is transferred to the manipulation platform and fixed in place using the custom-designed holder to minimize movement through the head bar.

Rat craniotomy

Sprague-Dawley (SD) rats (~300 g) are anesthetized with isoflurane in an induction chamber and then transferred to the surgical table for craniotomy. Anesthesia is maintained throughout the procedure using an RWD anesthesia machine (isoflurane level: 3; carrier air flow: 0.8). Ophthalmic ointment is applied to prevent corneal drying, and body temperature is maintained with a thermostatically controlled heating blanket, as in the mouse surgery. The scalp is shaved and incised to expose the skull, and the head is stabilized using ear bars to provide a mechanically stable environment for subsequent craniotomy. A craniotomy with a diameter of approximately 5 mm is opened over the target region. The brain surface is continuously irrigated with aCSF to maintain moisture. The dura is then gently opened using a bent needle tip from a 1 mL syringe under visual guidance to allow micropipette access.

Marmoset craniotomy

Marmosets are anesthetized with isoflurane in an induction chamber and then transferred to the surgical table for craniotomy. Anesthesia was maintained throughout the procedure using an RWD anesthesia machine (isoflurane level: 4; carrier air flow: 0.8). Body temperature was maintained around 37 °C with a thermostatically controlled heating blanket. The scalp was incised to expose the skull, and the head was stabilized to provide a mechanically stable environment for the craniotomy. A craniotomy with a diameter of approximately 8 mm is opened over the target region. The brain surface was continuously irrigated with artificial cerebrospinal fluid (aCSF) to maintain moisture, and the dura was gently opened under visual guidance to allow micropipette access.

Post-operative care

After the experiments, animals were monitored and cared for by a licensed veterinarian and received appropriate postoperative analgesics and antibiotics via injection to minimize pain and prevent infection.

Patch clamp electrophysiological recording procedures

Two in vivo electrophysiological recording configurations are performed: cell-attached and whole-cell patch-clamp. In both cases, the essential prerequisite is the formation of a tight and stable gigaseal between the micropipette tip and the cell membrane. Micropipette tip geometry and pressure control are two key practical factors influencing gigaseal longevity. In terms of tip geometry, a smaller aperture generally facilitates seal formation and improves stability. However, if the opening is too small, it becomes more susceptible to clogging by tissue debris in vivo, which can reduce sealing efficiency. In practice, we therefore target an aperture of approximately 1 μm as a compromise between sealability and robustness. The tip taper angle also affects both sealing and tissue interaction: a larger taper can promote seal formation, but it also tends to increase tissue disruption and causes the shank to thicken rapidly, which can limit insertion depth and reduce the available workspace. Conversely, an excessively fine taper compromises mechanical robustness and increases the likelihood of tip damage. Based on these considerations, we use a taper angle of approximately 2–3° as a practical balance. Pressure control is similarly critical for reliable gigaseal formation and maintenance. In typical operation, positive pressure is released rapidly during sealing, followed by a transition to controlled, steady suction. Excessive suction can rupture the membrane and cause seal failure, whereas insufficient suction may lead to loss of contact and unstable sealing. Empirically, a negative pressure in the range of -15 to -40 hPa is often effective in our setup.

In the cell-attached recording configuration, the neuronal membrane patch at the micropipette tip remains intact, avoiding disruption of the intracellular environment. To maintain physiological conditions, the micropipette is filled with a solution having the same composition as the aCSF. This configuration enables the recording of spontaneous neuronal firing. In this mode, the command potential V_0 is adjusted such that no net current flows through the patch[30]. When the micropipette tip targets the neuron precisely, it can enable the good contact with the neuronal membrane and form a tight seal, such that the command potential V_0 approximates the resting membrane potential V_m. In contrast, poor targeting accuracy leads to a significant deviation of V_0 from V_m; typically, V_0 shifts closer to 0 mV due to the weak seal information and elevated leak conductance. Thus, V_0 serves as an indicator of targeting accuracy: a V_0 value closer to V_m denotes higher targeting accuracy, while values approaching 0 mV suggest inferior seal quality caused by poor targeting.

In the whole-cell recording mode patch clamp operation, the aspirated membrane patch is ruptured by applying negative pressure through the micropipette, allowing the electrode solution to directly access the intracellular environment. In this state, the current flowing through all ion channels in the whole cell membrane can be measured. The above recording state is therefore named the whole-cell mode. To maintain physiological conditions, the micropipette is filled with an intracellular solution containing (in mM): 120 K-gluconate, 8 KCL, 8 HEPES, 0.2 EGTA, 4 Mg-ATP (pH adjusted to 7.2-7.3 with KOH, and the osmolarity is adjusted to 285-290 mOsm/kg with glucose). A tight and stable gigaseal between the micropipette tip and the cell membrane is essential for achieving stable whole-cell recordings. This configuration enables direct measurement of the neuron's resting membrane potential, membrane resistance, and action potentials.

Results

In this chapter, we first obtained the calibrated micropipette resistance-distance model using FEM simulations. Next, we evaluated the performance of the proposed filtered method MDF-WFLC-KF on the offline in vivo current recordings contaminated by noise, and compared it with two advanced nonlinear filtering approaches, the Extended Kalman Filter (EKF) and the MDF-WFLC. Subsequently, we validated the effectiveness of the developed sensing method using cells from acute brain slices, where the micropipette was driven with periodic displacements to mimic the relative motion of cells in vivo. Finally, we integrated both the filtering and sensing methods into a conventional patch-clamp system and designed a robotic in vivo patch clamp operation process with a new approach strategy. The performance of this robotic system was evaluated through in vivo electrophysiological recordings in anesthetized, head-fixed mice, rats, and marmosets.

Calibration results of the micropipette resistance model by FEM modeling

Figure 3c presents an approaching simulation result, in which the micropipette is located at 0.5 μm away from the sample, and the micropipette resistance is 9.53 MΩ, an increase from 8.01 MΩ (finite away from the sample). The sample surface undergoes deformation due to the flow of the fluid from the micropipette tip. The fluid flow of the micropipette outlet is caused by the pressure applied to the micropipette inlet, which is a common operation to prevent the blockage of the micropipette tip during in vivo manipulation.

The theoretical analysis in section "Micropipette resistance modeling for distance estimation" shows that the outer radius r_o, inner radius r_i, Young's modulus E, and injection pressure (P) are the factors influencing $R_a(d)$. To establish an accurate model of access resistance as a function of tip-membrane distance. We performed a series of FEM simulations to calibrate the coefficients k_1, k_2, and n, as well as the function sf in Eq. (8). In these simulations, the tip-membrane distance was systematically varied from 0.3 μm to 6 μm.

Firstly, we quantified the variation in access resistance over a tip-membrane distance range of 0.3-6 μm under five different Young's moduli ($E = 500$ Pa, 1000 Pa, 2000 Pa, 4000 Pa, and ∞ Pa). In these simulations, the injection pressure was fixed at $P = 100$ Pa, the micropipette outer radius was $r_o =$ 0.8 μm, and the inner radius was $r_i =$ 0.5 μm, as shown in Fig. 4a. There is a turning point on the access resistance as the distance between the micropipette opening and the neuronal membrane decreases. The distance corresponding to this turning point shifts to smaller values with increasing Young's modulus and asymptotically approaches zero as the Young's modulus tends to infinity. This resistance behavior can be attributed to membrane deformation effects: when the micropipette approaches the membrane at close proximity, the outlet flow generates elevated local pressure, causing membrane deformation that exceeds the nominal change in tip–membrane distance. As the Young's modulus increases, membrane deformation becomes progressively more difficult to induce, resulting in a reduced deformation magnitude and consequently shifting the turning point to a smaller separation distance.

Then we conducted a second set of simulations to evaluate the variation in access resistance as a function of the tip-membrane distance under different injection pressures (0 Pa, 100 Pa, 200 Pa, 300 Pa, and 400 Pa). In contrast to the effect of Young's modulus, increasing the injection pressure leads to a shift of the tuning point toward larger tip-membrane distance, as shown in Fig. 4b. This behavior can be readily understood by considering that a higher injection pressure produces a greater outlet flow velocity, which in turn exerts a stronger hydrodynamic force on the membrane, resulting in more pronounced membrane deformation. Consequently, for the same nominal tip–membrane separation, a higher outlet velocity induces a larger membrane deflection, effectively increasing the actual tip–membrane distance and thereby reducing the measured access resistance.

Furthermore, we conducted FEM simulations to investigate the effect of the micropipette outer radius (r_o) on the access resistance as a function of tip-sample distance. As shown in Fig. 4c, with the inner radius fixed at 0.5 μm and under a constant injection pressure of 200 Pa, the access resistance increases with increasing r_o. In addition, FEM simulations were performed to examine the effect of the inner radius (r_i) on the variation of access resistance with tip-sample proximity. The access resistance-distance relationships for five different inner radii (0.3 μm, 0.4 μm, 0.5 μm, 0.6 μm, and 0.7 μm) are shown in Fig. 4d. As expected, smaller micropipette openings result in higher access resistance values. Based on the analysis of these simulation data, we identified the model that describes the access resistance as a function of the tip-membrane distance by fitting the simulation results using a least-squares method ($R^2 > 0.99$), as follows:

$$R_a(d) = \frac{\rho}{0.65\pi\left(d + \frac{0.165P+0.188}{(0.682E+4.395)d}\right)^{1.2}} \ln\left(\frac{\mathrm{r_o}}{\mathrm{r_i}}\right) + \frac{\rho}{4.34\mathrm{r_i}} \tag{24}$$

Correspondingly, the micropipette resistance can be expressed as follows:

$$R(d) = \frac{\rho}{0.65\pi\left(d + \frac{0.165P+0.188}{(0.682E+4.395)d}\right)^{1.2}} \ln\left(\frac{\mathrm{r_o}}{\mathrm{r_i}}\right) + \frac{\rho}{4.34\mathrm{r_i}} + \frac{\rho}{\mathrm{r_i}\pi\tan(\theta)} \tag{25}$$

To validate the effectiveness of the numerical model, we compared the calculated $R - d$ curve for a given parameters ($r_o/r_i = 1.5, E \approx 1GPa$, and $P = 10$hPa) with that obtained from petri dish bottom. We matched the numerical models to experimental data by offsetting the vertical position d_0. A nearly perfect match between experiments and numerical model calculations is achieved with the mean squared error of 0.099 MΩ, in the distance range larger than 0.3 μm, as shown in Fig. 4e.

The numerical model not only predicts the distance behavior of access resistance but also provides a method to measure the Young's modulus of approached samples. We performed approaching experiments on hippocampus neurons in brain slices, adherent cells (HEK 293), and petri dish substrates. In each experiment, a constant pressure of 20 hPa was applied. The geometry parameters of the micropipette used for the estimation of Young's modulus were characterized using SEM. The measured Young's modulus of the three samples was 0.71 ± 0.17 kPa, 1.54 ± 0.46 kPa, > 1 GPa (average ± standard deviation), respectively (Fig. 4f). These results fall within

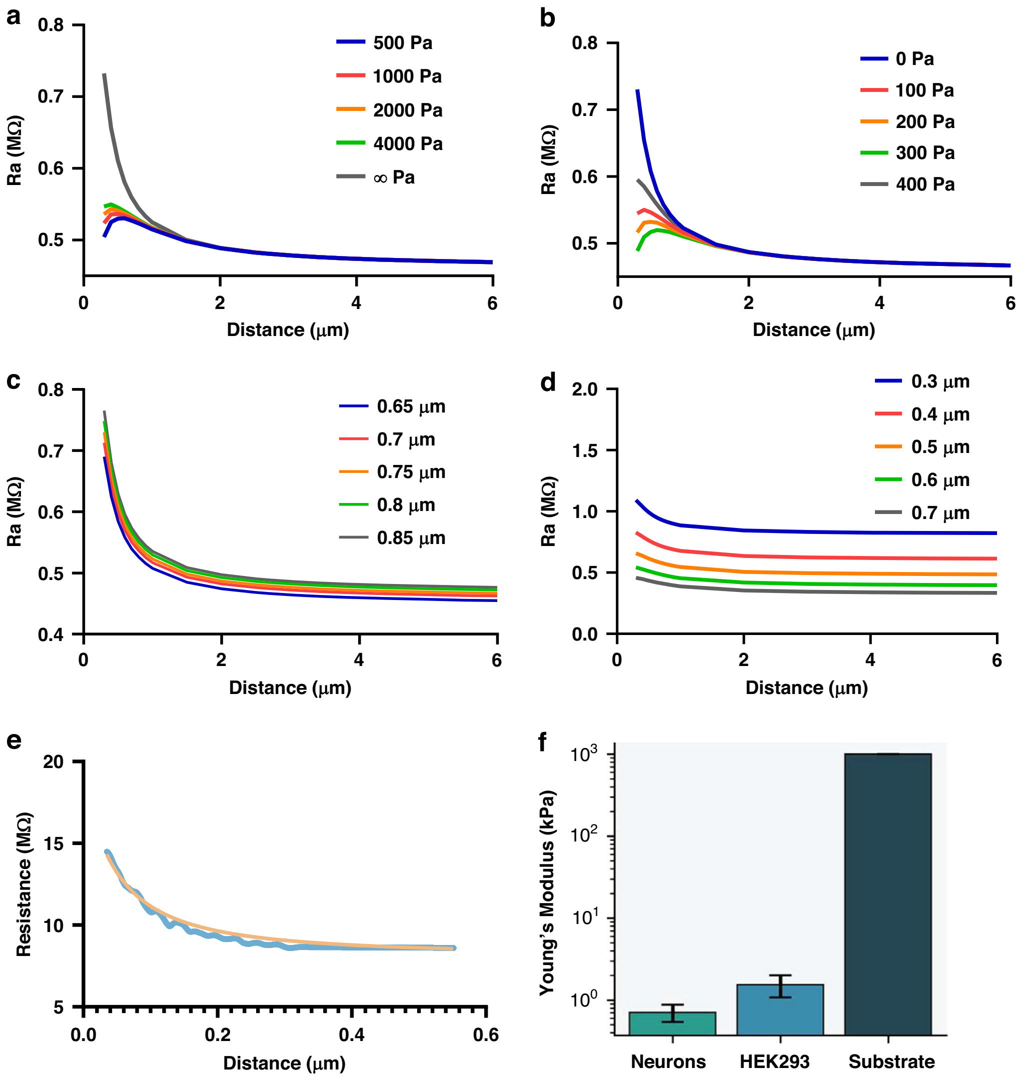

Fig. 4 Calibration results for the micropipette resistance-distance model. a Variation of access resistance with tip-cell distance for different membrane Young's moduli. **b** Variation of access resistance with tip-cell distance at different injection pressures. **c** Variation of access resistance with tip-cell distance at different outer radii. **d** Variation of access resistance with tip-cell distance at different inner radii. **e** Comparison of theoretical and experimental resistance changes during approach to the HEK293 cell membrane (blue: experimental results; yellow: calculated results). **f** Estimation of the Young's modulus of three samples (neurons in acute brain slices, HEK293, and petri dish substrate) using the proposed resistance-distance model

the expected orders of magnitude reported in the literatures, with neuronal cells typically exhibiting moduli on the order of 10^{-1}- kPa, HEK293 cells around 1 kPa, and conventional tissue-culture plastics in the gigapascal range[27,31,32].

Validation results of the MDF-WFLC-KF method

Due to the lack of a tight seal between the micropipette tip and the cell membrane before gigaseal formation, environmental electrical noise in the measured micropipette resistance can distort resistance-based tip-to-membrane distance estimation, compromising the accuracy of the localization method. The gray trace in Fig. 5a shows a representative current recording acquired with the micropipette positioned near a cell under voltage clamp at −70 mV. Fast Fourier Transform (FFT) analysis of the recording revealed two dominant frequency components at approximately 1 Hz and 4 Hz, as shown in Fig. 5b. In addition, time–frequency analysis (inset in Fig. 5b) confirmed that these frequency components persist throughout the recording, indicating that they are intrinsic to physiological tissue motion rather than transient noise artifacts.

To achieve accurate proximity measurement between the neuron and the micropipette tip, it is essential to effectively suppress noise in the recorded micropipette

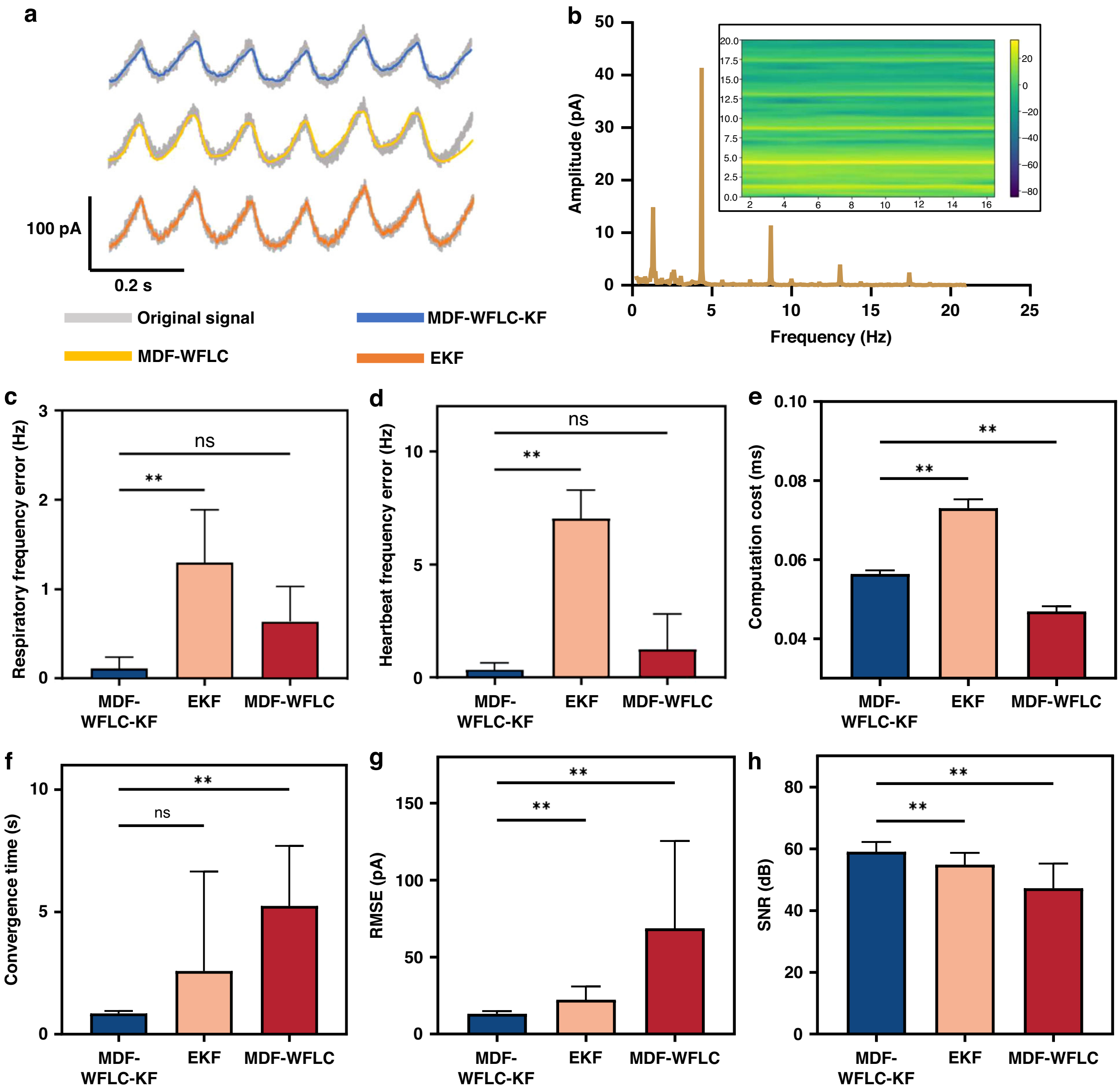

Fig. 5 Signal characteristics and validation of the proposed MDF-WFLC-KF method. a Representative current recording (gray trace) obtained when the micropipette was positioned near a neuron under voltage clamp at −70 mV, together with the filtering results achieved by the proposed MDF-WFLC-KF, MDF-WFLC, and EKF algorithms. The raw trace exhibits environmental noise and periodic fluctuations associated with physiological motion, while the filtered traces illustrate the denoising effectiveness of each algorithm. **b** Fast Fourier Transform (FFT) spectrum of the recorded signal reveals two dominant frequency components at approximately 1 Hz and 4 Hz. The corresponding subfigure presents a time-frequency analysis, which confirms that these dominant frequencies persist throughout the recording period. **c**, **d** Comparison of frequency estimation errors among three filtering methods. The MDF-WFLC-KF algorithm exhibited lower estimation errors for both dominant frequencies compared with EKF and MDF-WFLC. **e** Comparison of computational efficiency among the three filtering methods. The MDF-WFLC-KF algorithm achieved an average processing time of 0.056 ms per signal, lower than that of EKF (0.073 ms) and higher than MDF-WFLC (0.048 ms). **f** Comparison of convergence times among three filtering methods. EKF achieved the shortest average convergence time (0.39 ± 0.108 s, excluding two outliers), followed by MDF-WFLC-KF (0.846 ± 0.108 s), which remained acceptable for in vivo applications. In contrast, MDF-WFLC required the longest convergence time (~5 s) to track the real signal, increasing the risk of missing target cells. **g** Comparison of RMSE among three filtering methods. The MDF-WFLC-KF algorithm achieved the lowest RMSE (13.085 ± 1.86 pA) compared with EKF (22.208 ± 8.684 pA) and MDF-WFLC (68.681 ± 56.777 pA). **h** Comparison of SNR among three filtering methods. The MDF-WFLC-KF algorithm achieved the highest SNR (59.07 ± 3.192 dB), higher than that of EKF (54.865 ± 3.879 dB) and MDF-WFLC (47.258 ± 7.987 dB)

current. To evaluate the proposed filtering algorithm's effectiveness, four criteria, including signal-to-noise ratio (SNR), root mean square error (RMSE), computation cost per signal, and convergence time, are considered. The SNR reflects the quality of the filtered signal. A higher SNR means less noise, demonstrating the filter's effectiveness in noise reduction. The RMSE is another metric used to evaluate filtering performance. It measures the root mean square error between the filtered signal and the ground truth signal. A lower RMSE indicates that more details of the original signal are preserved. Since the ground truth data is unknown, in this work, we used a 4th-order low-pass Butterworth filter with a cutoff frequency of 20 Hz and zero-phase compensation to obtain the ground truth signal from the original data. The computation cost per signal measures the algorithm's computational complexity. A lower cost indicates better real-time performance, allowing the method to more accurately sense neuronal motion. Convergence time measures the filter's ability to track data. A shorter convergence time allows the algorithm to follow neuron motion more quickly, reducing the risk of missing target neurons.

We tested on eight offline current data segments, which are sampled at 1 kHz from eight different in vivo experiments. They are recorded when the micropipettes are nearby target neurons, showing quasi-periodic characteristics. To demonstrate the effectiveness of our proposed filter algorithm, we compared filtered results to those obtained from EKF[33] and MDF-WFLC filter algorithms. The MDF-WFLC algorithm was included as a comparative baseline to clarify that the proposed method is not a simple modification of the WFLC framework. Instead, by incorporating a Kalman filter, the proposed approach enables rapid identification of linear parameters, thereby significantly improving filtering accuracy. The parameter settings of MDF-WFL-KF, EKF, and MDF-WFLC algorithms are provided in Supplementary information. It should be noted that, for a fair comparison, the parameters of all algorithms were optimized beforehand and kept constant across different test signal segments. Eight independent data segments were evaluated under these fixed conditions. A representative filtered result is shown in Fig. 5a. The signal filtered by MDF-WFLC-KF (blue line) shows a closer match to the original signal and exhibits smoother variations compared with those obtained using MDF-WFLC (yellow trace) and EKF (orange line).

The results showed that our method can accurately estimate the multiple dominant frequencies of the original signal compared with other filtering algorithms. The results show no significant difference between the frequencies estimated by our method (frequency 1: 1.20 ± 0.57 Hz; frequency 2: 7.19 ± 1.07 Hz) and those obtained from Fast Fourier Transform (FFT) (frequency 1: 1.30 ± 0.58 Hz; frequency 2: 7.05 ± 1.26 Hz), with P-values greater than 0.05 (0.055 and 0.47, Wilcoxon signed-rank test). Moreover, MDF-WFLC-KF achieved lower estimation errors (frequency 1: 0.16 Hz and frequency 2: 0.45 Hz, RMSE) compared with the MDF-WFLC method (frequency 1: 0.74 Hz; frequency 2: 1.92 Hz). By contrast, EKF failed to provide reliable estimates (frequency 1: 0.0049 ± 0.0061 Hz; frequency 2: 0.0093 ± 0.0061 Hz), with significant differences from FFT (P-value $= 0.0078$ for both frequencies, Wilcoxon signed-rank test), as shown in Fig. 5c, d.

For signal accuracy, MDF-WFLC-KF achieved the lowest RMSE (13.085 ± 1.860 pA) compared with other methods (EKF: 22.208 ± 8.684 pA, $P = 0.0078$; MDF-WFLC: 68.681 ±56.777 pA, $P = 0.0078$, Wilcoxon signed-rank test). The comparison result is shown Fig. 5g. MDF-WFLC-KF also outperformed the others in terms of SNR. The SNR of signals filtered by our method was 59.070 ± 3.192 dB, significantly higher than that of EKF (54.865 ± 3.879 dB, $P = 0.0078$), and MDF-WFLC (47.258 ± 7.987 dB, $P = 0.0078$), as shown in Fig. 5h. Regarding computation cost, our method required an average of 0.056 ms per signal, which is lower than EKF (0.073 ms), as shown in Fig. 5e. Although this is higher than MDF-WFLC (0.047 ms), it still meets real-time requirements. In terms of convergence time, EKF achieved the shortest average (0.390 ± 0.108 s, with two outliers ignored). MDF-WFLC-KF showed a higher convergence time (0.846 ± 0.108 s), but remained suitable for in vivo experiments. By contrast, MDF-WFLC required the longest convergence (~5 s) to track the real signal, often resulting in a high risk of missing target cells, as shown in Fig. 5f.

Validation results of the real-time localization method in acute brain slices

To validate the accuracy of the proposed localization method, we conducted experiments in acute brain slices, in which cell motion was simulated by driving the micropipette with periodic displacements to mimic in vivo physiological movements. Two representative motion profiles were designed to emulate neuronal movements under different physiological conditions:

$$m_1(t) = k_a \sin\left(2\pi f_1 t - \frac{\pi}{2}\right) + 2k_a \tag{26}$$

$$m_2(t) = k_a \sin\left(2\pi f_1 t - \frac{\pi}{2}\right) + k_b \sin(2\pi f_2 t) + 2(k_a + k_b) \tag{27}$$

where $k_a = \mu\text{m}$ and $k_b = 0.8\mu\text{m}$. The offsets $2k_a$ and $2(k_a + k_b)$ were added to keep the commanded displacement positive and avoid driving the piezoelectric stage into negative displacement. The first motion profile, a single-frequency sinusoidal, models neuronal motion in anesthetized mice, where cardiac pulsation dominates, and respiration-induced displacement is relatively small under stable anesthesia. The second motion profile, a superposition of two sinusoids, mimics neuronal motion in rats or marmosets, where both heartbeat and respiration contribute substantially to the overall displacement.

In the experiments, no vision feedback was available to determine the initial distance between the neuron and the micropipette tip. A previous study reported that a micropipette resistance increase of approximately 0.3 MΩ indicates a contact between the micropipette and the cell membrane[34]. Therefore, once the micropipette resistance increases by 0.3 MΩ, the micropipette was retracted by a distance greater than $2k_a$ or $2(k_a + k_b)$µm, but less than 10 µm, which falls within the valid operating range of the proposed localization model. After this adjustment, the micropipette was driven with the periodic motion profiles to simulate dynamic neuronal motion. Two representative resistance traces and their corresponding filtered signals are shown in Fig. 6a, b. Five micropipettes were used for each experiment. The estimated proximity distance and the ground-truth relative motion amplitude are shown in Fig. 6c, d, demonstrating close agreement. Root mean square error (RMSE) was employed to evaluate the accuracy of the proposed system. The tracking errors were 0.41 ± 0.07 µm and 0.45 ± 0.10 µm for the single- and dual-frequency motion tests, respectively (Fig. 6e). Welch's t-test indicated that the difference between the two trajectories was not statistically significant ($p = 0.543$), suggesting stable tracking performance under both motion patterns. Together, these results demonstrate high tracking precision and robustness across different trajectory conditions, supporting the effectiveness of the proposed localization method for accurate distance estimation.

Results of phase-synchronized capture for dynamically moving cells in vivo

To assess phase-synchronized capture strategy, we conducted in vivo capture experiments in anesthetized mice using 40 micropipettes, with 10 trials for each phase. During each trial, the presence of a nearby cell was first confirmed by a quasi-periodic change in micropipette resistance, indicating that the tip was within range of a moving cell. After identifying a candidate cell, the micropipette was advanced according to the estimated proximity distance and the specified phase, and negative pressure was then applied to attempt gigaseal formation with the neuronal membrane.

Micropipette resistance measured after applying negative pressure was used to evaluate the capture performance. Higher resistance indicates better capture, and a resistance >1000 MΩ is considered as a successful gigaseal, which is required for subsequent transmembrane voltage and current recordings by electrically isolating the external electromagnetic noise. The capture tests showed that contacting the cell at FP yielded the best performance, with an average final resistance of 1342.04 ± 405.74 MΩ (Fig. 6f). In contrast, the final resistance at the other phases was substantially lower: 24.38 ± 13.28 MΩ at NP, 112.98 ± 15.71 MΩ at AP, and 347.24 ± 58.76 MΩ at TP. Quantitatively, the final resistance at FP was approximately 55-fold, 12-fold, and 4-fold higher than those at NP, AP, and TP, respectively. Dunnett's multiple-comparison test further confirmed that resistance at FP was significantly higher than at NP, AP, and TP (adjusted $p < 0.0001$), demonstrating the effectiveness of the proposed capture strategy.

After phase-synchronized capture for dynamically moving cells in vivo, the micropipette position was held constant. Because the cell may continue to exhibit residual axial motion after capture, the relative tip-membrane indentation may increase and could, in principle, affect membrane integrity. However, our experimental observations suggest that this effect is limited under our conditions. To further evaluate this safety concern, we performed validation experiments in acute mouse brain slices, where the neuron is relatively stationary, and the relative axial motion is primarily introduced by the micropipette. After initial membrane contact, we advanced the micropipette toward the cell by up to approximately 10 µm, which exceeds the measured amplitude of neuronal motion. Under these conditions, we were still able to subsequently form a gigaseal and obtain stable electrophysiological recordings, indicating that this level of relative axial approach did not measurably compromise membrane integrity or recording quality in our setup.

Robotic in vivo patch-clamp results in mice

We integrated the localization method and phase-synchronized capture strategy into an existing manual patch-clamp system, establishing a robotic patch-clamp manipulation workflow. To validate the effectiveness of the established system, we performed patch-clamp recordings in the brains of living mice. In the experiments, 80 micropipettes were used across 8 mice.

Figure 7a illustrates the resistance profile during a successful capture process using the proposed method. In the figure, current changes are used to represent resistance variations. This choice allows for a clearer visualization of small fluctuations at low resistance and the rapid resistance increase during sealing. Displaying resistance directly would obscure these low-resistance dynamics due to the high-resistance values associated with successful seal formation. The micropipette was initially lowered at a speed of 10 µm/s and halted at the target depth of 50 µm.

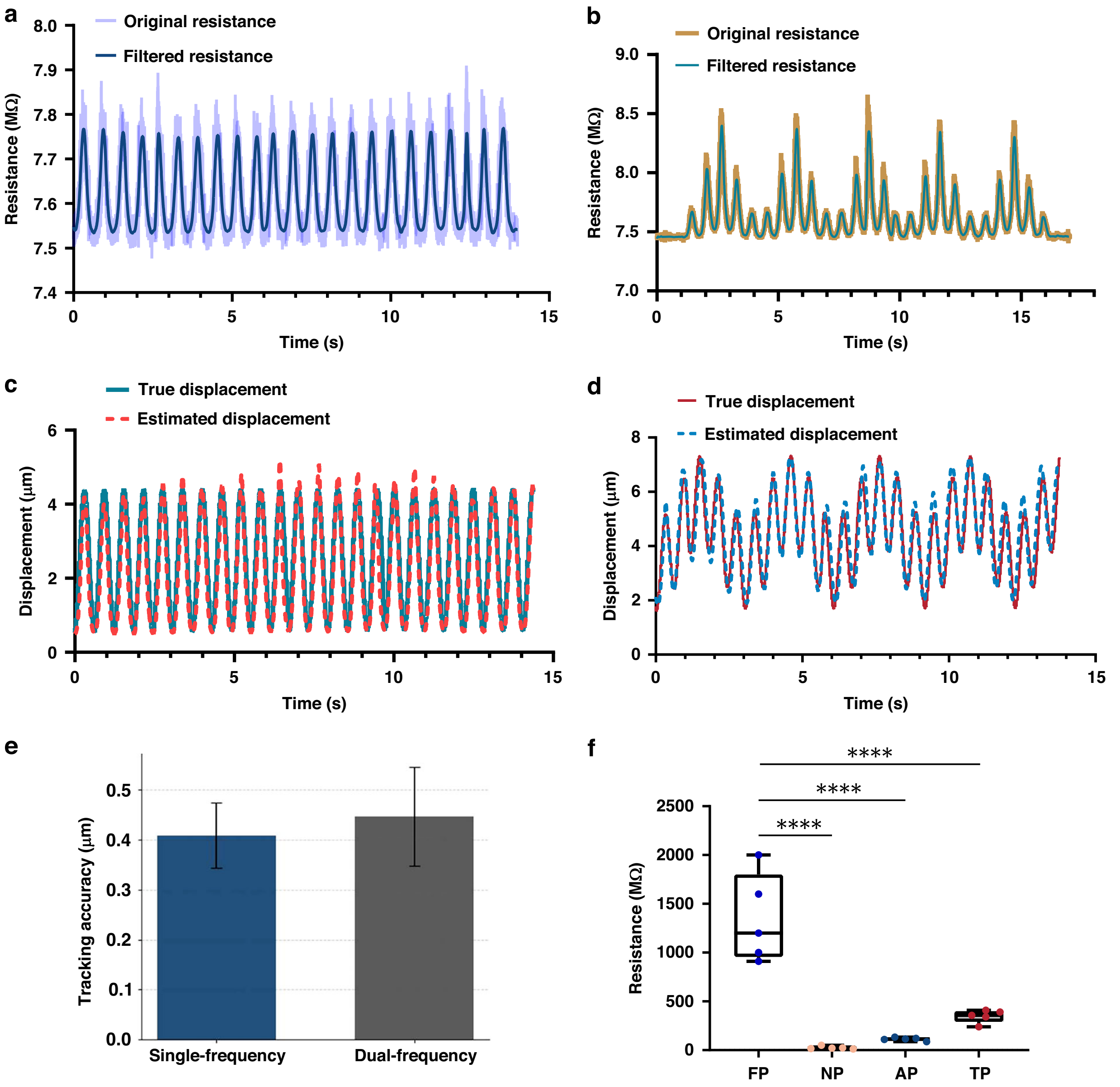

Fig. 6 Validation of the proposed localization method and phase-synchronized capture strategy. a, b Representative resistance traces obtained under two motion profiles: single-dominant-frequency and dual-dominant-frequency motion, respectively. **c**, **d** Comparison between the estimated proximity changes and the commanded micropipette displacements shows close agreement. **e** Tracking errors under the two motion conditions. The tracking errors were 0.41 ± 0.07 μm and 0.45 ± 0.10 μm for the single- and dual-frequency motion tests, respectively. **f** Comparison of four capture strategies. Contacting the cell at FP yielded the highest gigaseal resistance, achieving an average final resistance of 1342.04 ± 405.74 MΩ. In contrast, the final resistances at other positions were significantly lower: 24.38 ± 13.28 MΩ at NP, 112.98 ± 15.71 MΩ at AP, and 347.24 ± 58.76 MΩ at TP

It then performed cell searching at a reduced speed of 1 μm/s. The micropipette position profile is shown in the middle panel of Fig. 7a. When a quasi-periodic resistance fluctuation was detected, it was considered indicative of encountering a cell. To enable online parameter identification, the micropipette was consecutively lowered in three 1 μm steps, and the resulting resistance changes were recorded to characterize uncertainties arising from unknown micropipette geometric parameters. Once these parameters were determined, the distance between the micropipette and the cell could be estimated, as shown in the bottom panel of Fig. 7a. The capture strategy was then initiated, ultimately achieving precise attachment of the micropipette to the cell and formation of a gigaseal, as

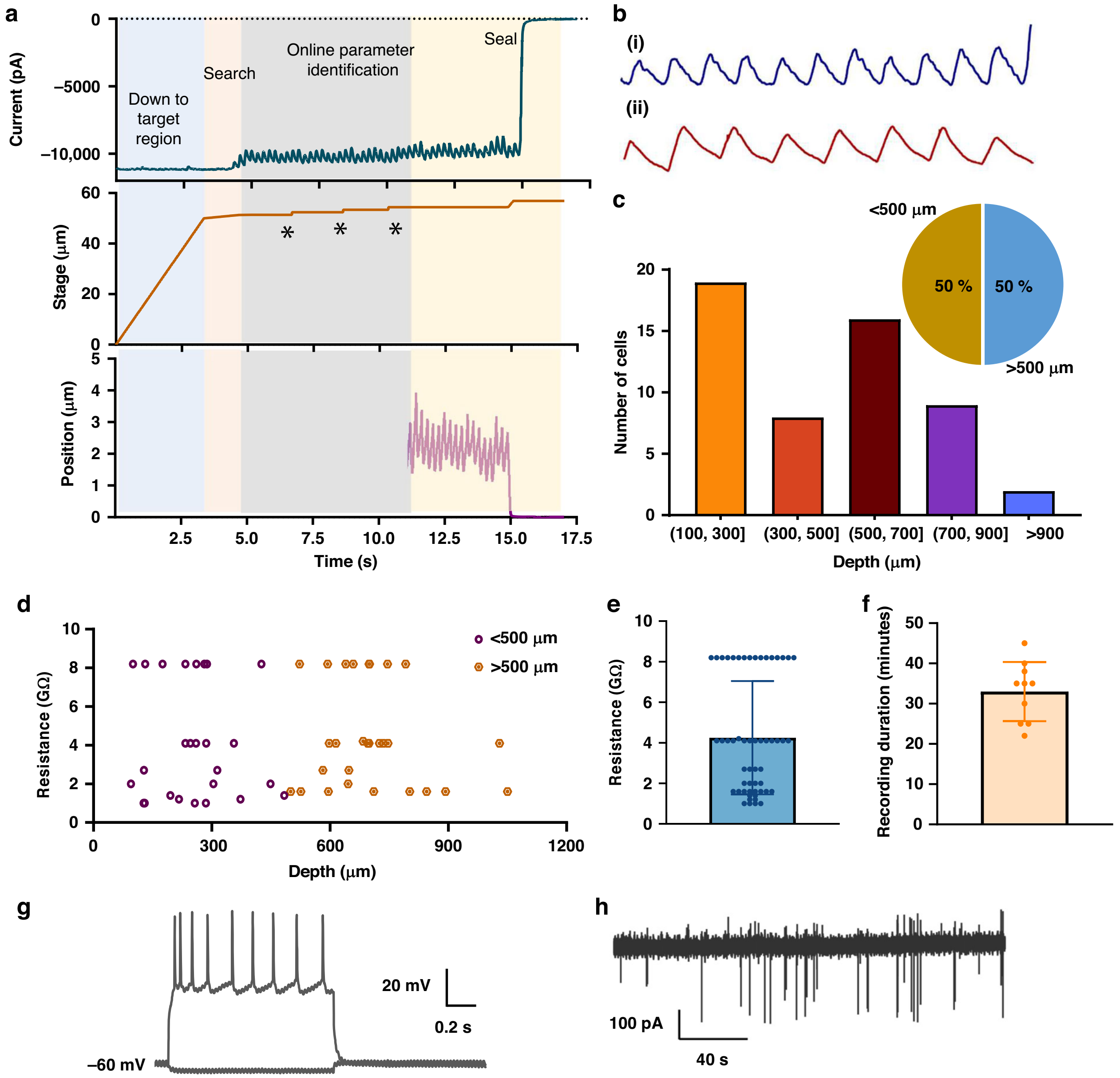

Fig. 7 In vivo robotic patch-clamp results in anesthetized mice. a A representative current trace (top), micropipette motion trajectory (middle), and estimated tip-membrane distance (bottom) during a successful capture using the proposed method. The blue shaded region indicates rapid micropipette descent to the predefined depth. The pink shaded region denotes low-speed cell search. The gray shaded region indicates that a neuron was detected at the micropipette tip opening based on resistance fluctuation; three consecutive stepwise descents (each by one depth increment, marked by asterisk) were then executed to perform online identification of the electrode resistance model. In the yellow shaded region, the system used the online-identified micropipette resistance model to estimate the neuronal motion dynamics and performed a precise capture procedure. **b** Enlarged current traces for two encounter scenarios. (i) When the micropipette encounters a blood vessel, the resistance waveform exhibits fine ripples and additional high-frequency components, reflecting the periodic pulsation of the vessel wall and the dynamics of surrounding tissue. (ii) In contrast, when encountering a neuron, the resistance waveform remains smooth. **c** Gigaseal formation frequency in superficial and deeper brain regions. The inset pie chart shows comparable gigaseal likelihood in superficial (<500 μm) and deep (>500 μm) regions (40 trials per group). **d** Distribution of gigaseal resistance across manipulation depths. **e**, **f** Summary of seal resistance and seal duration achieved by the proposed system, with an average resistance of 4.25 ± 2.77 GΩ and an average duration of 33 ± 7 minutes. **g** Representative whole-cell patch-clamp recordings showing evoked firing responses to current injections of −20 pA and +50 pA. **h** Representative cell-attached recordings showing spontaneous firing activity

Table 1 Comparison across three robotic patch-clamp systems

	Autopatcher[35]	Autonomous Autopatcher[8]	Robotic in vivo micromanipulation system
Mice	16	14	8
Micropipettes	73	317	80
Not clogged	81%	66%	87.5% (70/80)
Cell detected	93%	95%	94.3% (66/70)
Gigaseal	51%	24%	81.8% (54/66)

illustrated in the yellow-highlighted region in the top panel of Fig. 7a. We also provide a Supplementary Video S1 to illustrate the robotic patch-clamp sealing process. In addition, other representative segments of raw current traces corresponding to successful seals are included in the Supplementary Information.

Regarding the resistance fluctuations, two special cases were observed in the experiments. Due to the random relative alignment between the micropipette tip and cell membrane, if the tip is positioned near the edge of the membrane, the fluctuation amplitude is limited. As the micropipette moves further downward, these fluctuations suddenly disappear, as shown in Video S2. In another case, when the micropipette encounters a blood vessel, the fluctuation persists, and the resistance continues to increase as the micropipette descends, as shown in Video S3. Unlike the neuron contact case, the resistance remains stable after the positive pressure is released and the negative pressure is applied, whereas contact with neurons causes the resistance to sharply rise to hundreds of megaohms (MΩs) or even gigohms (GΩs). It is vital to distinguish whether the micropipette encounters a cell or a blood vessel before releasing the positive pressure, as contacting a vessel may damage the micropipette tip. In our study, we found a clear difference in the resistance waveform between these two cases. When the micropipette approaches a blood vessel, the resistance trace exhibits small, rapid fluctuations superimposed on a larger periodic oscillation (Fig. 7b(i)), which originates from the vessel wall pulsation and local micro-movements. In contrast, when approaching a neuron, the resistance waveform appears smooth and stable without such fine ripples (Fig. 7b(ii)). Note that, for visualization purposes, resistance traces shown in Fig. 7b are low-pass filtered using a Butterworth filter with a 20 Hz cutoff frequency to highlight low-frequency signatures associated with neuron and vessel encounters. This filtering does not alter the underlying conclusions.

This distinction method is physically reasonable because the resistance fluctuation reflects the dynamic distance between the micropipette tip and the surrounding tissue. When the pipette approaches a blood vessel, the periodic pulsation of the vessel wall induces microscale motion of the surrounding tissue and fluid, producing additional high-frequency components in the resistance signal. These small ripples represent the superposition of rapid local movements on top of the main pulsation cycle. In contrast, when the pipette approaches a neuron, the surrounding tissue exhibits mainly slow, viscoelastic displacement synchronized with the overall brain motion, and the high-frequency components are largely filtered out by the damping properties of the neural tissue. Therefore, the smoothness of the resistance waveform near neurons and the presence of fine ripples near vessels are consistent with the distinct mechanical dynamics of these two types of targets.

The in vivo experiments demonstrated strong overall performance of our robotic patch-clamp system across the key stages of the pipeline. First, clogging events were observed in 10 micropipettes, indicated either by an initial resistance exceeding 10 MΩ or by vascular encounters. In these cases, the system achieved an unclogging success rate of 87.5%, which was not significantly different from the rates reported by the two prior robotic methods (81% and 66%). Second, cell detection was achieved in 94.3% of trials (66/70 micropipettes), which is comparable to the 93% and 95% reported by the other two robotic systems, with no statistically significant difference. Conditioned on successful cell detection, our robotic patch-clamp system achieved a gigaseal success rate of 81.8% (54/66 micropipettes). We compared the yield with previously reported robotic patcher yields (see Table 1), including an autopatcher (51%)[35] and an autonomous autopatcher (24%)[8], and found that our yield was significantly higher (Fisher's Exact test, p-value: 1×10^{-4} and 1.2×10^{-17}, respectively). Among the failure cases, cell detachment from the micropipette tip before seal stabilization was a major contributor to unsuccessful sealing, likely due to unstable tip-membrane contact under ongoing physiological motion. A promising improved strategy is to implement closed-loop control of the micropipette position to maintain stable membrane contact, thereby minimizing relative motion and promoting more reliable gigaseal formation.

To evaluate the efficiency of cell capture by our robotic system across unrestricted depths, we designed two experimental groups, each consisting of 40 micropipettes used for in vivo seal-formation trials. One group targeted superficial brain regions (<500 μm), whereas the other targeted deeper regions (>500 μm). Figure 7d presents the distribution of gigaseal resistance as a function of manipulation depth, with the horizontal axis indicating the micropipette descent depth and the vertical axis representing the measured seal resistance using the robotic patch-clamp system. The frequency of successful seal formation across depth ranges is summarized in Fig. 7c, where the inset pie chart shows that gigaseals were obtained with comparable likelihood in both superficial and deep brain regions. These results demonstrate that our method enables precise single-cell capture regardless of tissue depth. Furthermore, we quantified seal resistance and seal duration as shown in Fig. 7e, f. The results shown an average seal resistance of 4.25 ± 2.77 GΩ and an average seal duration of 33 ± minutes, with all gigaseals persisting for over 20 minutes, demonstrating the effectiveness of our robotic system. The recording durations achieved in our study are broadly consistent with typical in vivo patch-clamp performance under both manual and robotic operation. For example, average recording durations of ~ 22 min[8] and ~20 min[36] have been reported. Recordings of ~8-30 min are common in awake mice[20,37], and an average duration of ~45 min has been reported in anesthetized mice using Autopatching[38]. These comparable recording durations indicate that our robotic patch-clamp procedure is effective and can achieve in vivo gigaseal stability comparable to that of established patch-clamp approaches.

Figure 7g shows a typical neuronal firing activity in the whole-cell recording mode, with the resting membrane voltage of −60 mV, membrane resistance of 308.9 MΩ, and membrane capacitance of 33.3 pF. These physiological indicators of the neuronal membrane indicate the good whole-cell configuration formation. Typical firing activity recorded by cell-attached recording is shown in Fig. 7h, with recording current baseline of ~1 pA with command potential V_0 of −60 mV. In the cell-attached recording, when the seal is poor, there is leak current between the membrane and the micropipette tip, which requires additional voltage clamp to compensate for the leak current. Thus, a smaller current baseline indicates a good seal, demonstrating the good performance of our robotic system.

Robotic in vivo patch-clamp results in rats and marmosets

After establishing quantitative performance in anesthetized mice, we further evaluated the proposed resistance-based sensing framework in larger animals to assess its generalizability under different physiological motion profiles and surgical constraints.

We further performed in vivo patch-clamp recordings in anesthetized rats, as shown in Fig. 8a and Video S4. When a neuron entered the vicinity of the micropipette tip, the measured micropipette resistance exhibited pronounced quasi-periodic fluctuations (Fig. 8b), similar to those observed in mice (Fig. 7a). A magnified view of these fluctuations (top trace in Fig. 8c) reveals a superposition of two approximately sinusoidal components. The corresponding amplitude spectrum (Fig. 8d) confirms two dominant peaks: a slower oscillation at ~1.3 Hz that is consistent with respiration and a faster component at ~5.9 Hz corresponding to cardiac pulsation. Notably, unlike in mice, the respiration-related component in rats exhibited a larger spectral amplitude than the heartbeat-related component.

Using the proposed resistance-distance model, we estimated neuronal motion in the rat brain in real time (bottom trace in Fig. 8c). The respiration-related displacement reached up to ~10 μm, whereas the heartbeat-related component was smaller, typically ~2–3 μm. These magnitudes are consistent with prior in vivo measurements, which reported a dominant respiration component (10–30 μm) and a comparatively minor heartbeat contribution (2–4 μm)[18]. Guided by this distance feedback, we achieved gigaseal formation and obtained both cell-attached and whole-cell recordings (Fig. 8e, f), demonstrating the feasibility of the proposed sensing-and-guidance workflow beyond mice.

We further extended the proposed system to non-human primates (marmosets) and conducted in vivo patch-clamp experiments under both head-fixed anesthesia and awake conditions (Fig. 8g and Video S5). Representative resistance traces during cell encounters are shown in Fig. 8H (anesthetized) and Fig. 8i (awake). Frequency-spectrum analysis revealed two dominant physiological components in both conditions, as shown in Fig. 8j. Under anesthesia, the respiration-related peak was centered at ~0.2 Hz, while the cardiac-related peak was observed at ~3.5 Hz. In the awake state, the respiration-related peak shifted to ~0.4 Hz, whereas the cardiac component remained largely unchanged at ~3.4 Hz. These results indicate a higher respiration rate in awake marmosets (~2.5 s per breath) compared with the anesthetized condition (~5 s per breath).

Using the proposed resistance-distance model, we estimated the corresponding tip-to-membrane distance dynamics for both conditions (bottom panels of Fig. 8h, i), enabling quantitative characterization of neuronal motion in the marmoset brain. Under anesthesia, the respiration-guided neuronal displacement reached up to ~18 μm, whereas the heartbeat-induced displacement was much smaller, at approximately ~1 μm. In the awake condition, the respiration-guided displacement decreased to ~8 μm, while the heartbeat-related component remained near ~1 μm. Notably, although respiration was faster in the awake state, the respiration-related displacement

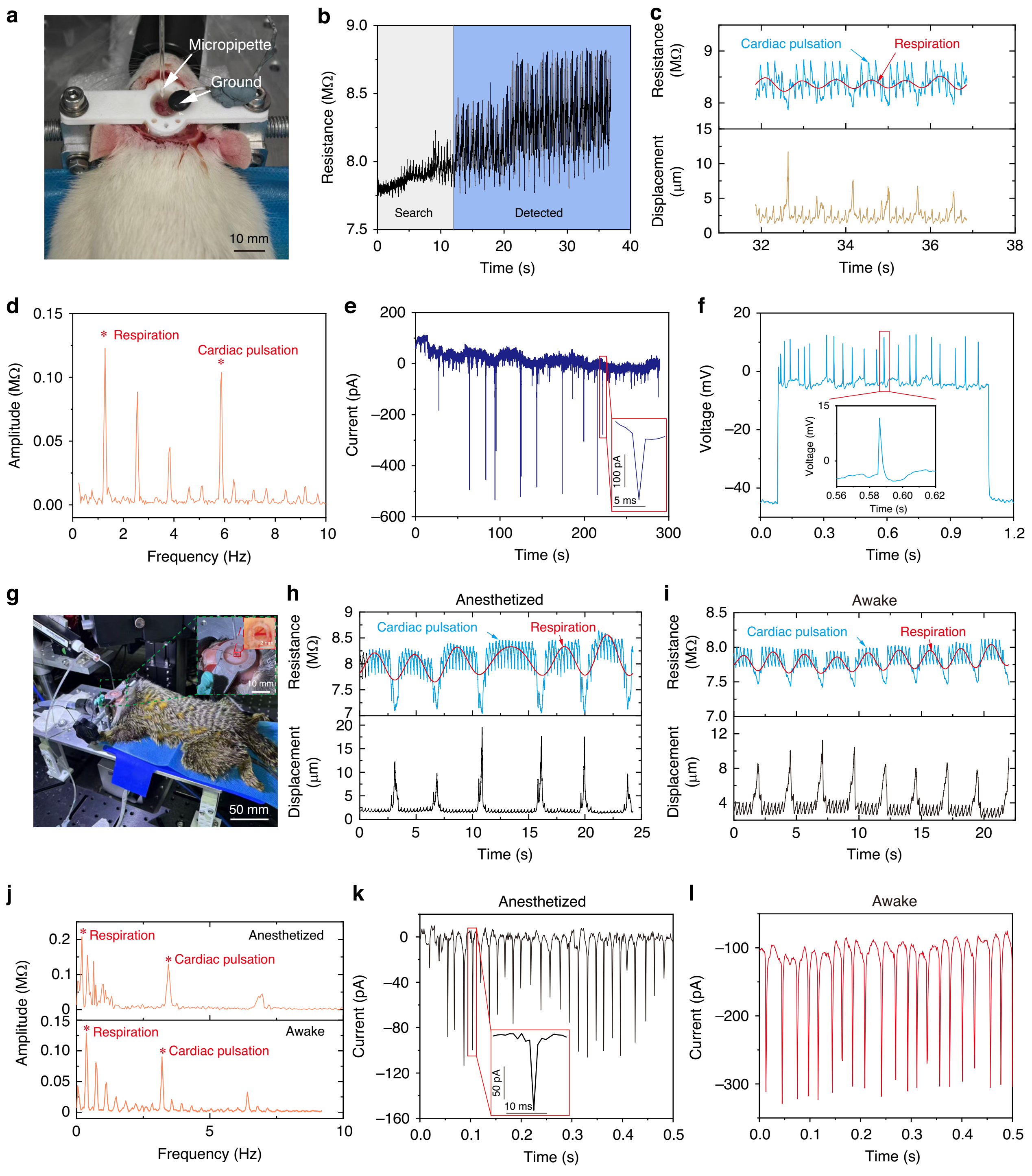

Fig. 8 In vivo robotic patch-clamp recording in anesthetized rats and in marmosets under anesthetized and awake conditions. **a** Photograph of the in vivo patch-clamp manipulation in rat. **b** Periodic micropipette-resistance fluctuations observed during micropipette descent upon encountering a neuron. **c** Zoomed-in resistance fluctuation near the cell (top) and the corresponding cell motion estimated using the proposed resistance-distance model (bottom). **d** FFT-based amplitude spectrum of the resistance signal, showing prominent peaks at ~1.3 Hz and ~5.9 Hz, corresponding to respiration- and heartbeat-related components, respectively. **e** Representative in vivo rat cell-attached recording. **f** Representative in vivo rat whole-cell recording. **g** Photograph of the in vivo patch-clamp manipulation in marmoset. **h** Marmoset (anesthetized): micropipette-resistance fluctuations near the cell (top) and estimated cell motion (bottom). **i** Marmoset (awake): micropipette-resistance fluctuations near the cell (top) and estimated cell motion (bottom). **j** FFT-based amplitude spectra of the marmoset resistance signals: anesthetized condition (top; dominant frequencies 0.2 Hz and 3.5 Hz) and awake condition (bottom; dominant frequencies 0.4 Hz and 3.4 Hz). **k** Representative marmoset cell-attached recording under anesthesia. **l** Representative marmoset cell-attached recording in the awake condition

amplitude was reduced, indicating that the magnitude of respiration-driven brain motion depends on factors beyond breathing frequency. The heartbeat-related component remained stable (~1 μm) across conditions, suggesting a comparatively minor and less state-dependent contribution. Based on the estimated cell motion, the operator achieved cell capture and gigaseal formation, yielding successful cell-attached recordings under both anesthetized and awake conditions (Fig. 8k, l). Whole-cell recordings were also obtained in these experiments.

Discussions

In this work, we propose a resistance-based model for the precise localization of dynamically moving cells in vivo. In our study, the dominant direction of cellular motion is assumed to be along the axial direction of the micropipette. This assumption is well justified for two reasons. First, from a biomechanical perspective, the craniotomy opening is located above the cortical surface. Consequently, most stress relaxation and pulsation-induced displacement propagate primarily along the depth (axial) direction, whereas lateral tissue deformation is substantially constrained by the surrounding cortical tissue and skull structures. As a result, axial motion dominates the micrometer-scale displacement transmitted to cells during physiological processes such as vascular pulsation and respiration. Second, previous two-photon imaging studies report that the lateral (XY) displacement of neurons is typically <2 μm[39]. Given that the neuronal soma size is approximately 10 ~ 20 μm[40], a lateral shift of <2 μm represents only a small fraction of the cell diameter and is unlikely to move the target cell completely out of the micropipette's effective interaction region during approach. In our framework, resistance sensing is primarily driven by the proximity between the micropipette tip and the cell membrane. Small lateral displacements may slightly alter the effective tip-cell geometry and thus modulate the measured resistance. Although axial motion dominates under typical in vivo conditions, extending this framework toward three-dimensional motion tracking could further broaden its applicability to scenarios involving complex tissue deformation. In future work, a three-dimensional measurement and modeling framework could be developed to more accurately characterize in vivo neuronal motion.

In our study, the resistance-distance relationship is treated as a low-dimensional parametric model whose key coefficients represent: (i) geometry-dominated effects associated with the micropipette, capturing how micropipette dimensions and taper contribute to baseline and distance-dependent resistance; and (ii) an effective interaction term that captures cell-to-cell variability in tip-membrane coupling, which is related to the membrane's effective Young's modulus. These coefficients can be identified online from the measured resistance response to known incremental displacements, allowing the system to automatically compensate for unknown micropipette-to-micropipette variation and adapt to differences across cells encountered in vivo. Importantly, this adaptive identification does not require explicitly specifying the cell type or assuming a fixed mechanical property across preparations. Instead, variations that affect the resistance-distance relationship are absorbed into an effective interaction parameter estimated from the real-time measurements. In this sense, the online identification step provides a general mechanism to accommodate variability in micropipette geometry and effective stiffness, thereby enhancing the reliability of resistance-based tracking and positioning under heterogeneous in vivo conditions. The resistance-distance model could be extended beyond distance tracking to infer a cell-specific mechanical parameter, such as an effective Young's modulus. In principle, this is feasible because the identified interaction coefficient is related to the membrane Young's modulus. However, recovering an absolute estimate of Young's modulus in vivo would require additional information and stronger identifiability conditions, such as independent measurements or constraints on the pressure term, as well as sufficiently informative excitation and measurements during online operation to ensure robustness to noise and model mismatch. Therefore, while the current method provides an adaptive "effective" interaction parameter that improves control robustness, extracting quantitative mechanical properties remains an interesting direction for future work.

In the current robotic manipulation workflow, even when a blood vessel can be identified (section "Robotic in vivo patch-clamp results in mice"), the micropipette typically retracts and re-enters through the cranial opening to avoid vascular structures. However, because the precise location and extent of the vessel are unknown, a trial-and-error lateral searching may still fail to circumvent the vessel, occasionally resulting in vessel puncture. Such events can lead to red blood cell leakage, occlusion of the micropipette opening, or damage to the micropipette tip, ultimately requiring micropipette replacement. Therefore, random lateral (XY) repositioning can substantially reduce procedural efficiency by increasing the number of trial moves, prolonging insertion time, and introducing unnecessary tissue disturbance. These observations motivate an important direction for future work: developing a proactive, closed-loop vessel-avoidance module. One promising approach is to formulate vessel avoidance as a local, resistance-guided navigation problem. Under this framework, when vascular contact risk is inferred from resistance feedback (such as a sustained elevation), the controller could (i) pause axial advancement, (ii) retract slightly to relieve contact, and

(iii) execute a minimal lateral "boundary-following" adjustment biased toward directions associated with decreasing resistance. After the resistance returns toward baseline, the system could resume axial advancement while gradually returning to the original insertion axis, thereby limiting lateral drift. To further reduce the number of exploratory lateral adjustments, another potential extension is to use sample-efficient sequential optimization (e.g., Bayesian optimization) to propose lateral offsets. By leveraging prior resistance measurements to prioritize candidate directions likely to reduce a resistance-based risk metric, this approach could replace inefficient random repositioning with structured, data-efficient exploration, reducing unnecessary lateral motion and lowering the probability of pipette damage and experimental failure.

Although the seal durations achieved in this study are broadly consistent with those reported in previous in vivo patch-clamp studies, achieving more stable, longer-duration recordings would be particularly beneficial for neuroscience experiments that require extended functional monitoring. Beyond optimizing electrode geometry and pressure-control protocols, maintaining a gigaseal over extended periods in vivo also requires accounting for persistent physiological perturbations, such as cardiac- and respiration-induced tissue motion, which can continuously disturb the tip-membrane interface and compromise seal stability. Therefore, an important direction for future work is to develop a closed-loop controller that actively regulates micropipette position to stabilize tip-membrane contact under ongoing physiological motion, thereby improving long-term gigaseal robustness.

Reported performance for imaging-guided robotic patch-clamp includes a seal success rate of approximately 46.6%, a time-to-seal of approximately 6 min, and an effective recording depth typically limited to <250 μm due to optical scattering constraints in cortical tissue[11]. In contrast, in our experiments, the proposed resistance-based system achieved a seal success rate of 81.8%, a mean time-to-seal of approximately 4 min, and a maximum recording depth of up to 1 mm. These results suggest that the blind resistance-based strategy offers advantages in terms of efficiency and depth of accessibility. We note, however, that the two approaches are designed for partially different experimental objectives. Two-photon-guided systems enable visual targeting of genetically or morphologically defined neurons, which is a significant advantage when cell-type specificity is required. However, such systems require complex optical setups, expensive hardware, such as a two-photon microscope, and are typically restricted to superficial cortical layers. In contrast, our method does not provide visual cell-type targeting but offers lower system complexity, reduced cost, and improved accessibility to deeper brain regions.

Beyond in vivo patch-clamp manipulation, the proposed robotic system may also be extended to other targeted in vivo single-cell operations[41]. Procedures such as single-cell electroporation, targeted microinjection, and aspiration-based extraction of cellular contents all critically depend on establishing and maintaining stable micropipette-cell contact in a dynamic in vivo environment. Notably, even when the micropipettes are filled with solutions different from those used in patch-clamp operations, or when their geometries vary, the system's online parameter identification enables adaptive modeling of the relationship between micropipette resistance and tip-membrane distance, thereby providing operators with actionable guidance for subsequent manipulations. As a result, our framework provides a generalizable solution for in vivo targeted single-cell manipulation, potentially lowering the barrier to enabling precise single-cell manipulations across modalities, species, and brain states.

Conclusions

In this work, we present a robotic patch-clamp system, which can estimate in vivo cell motion driven by intrinsic physiological activity using a micropipette resistance-based localization method and precisely capture target cells using a phase-synchronized capture strategy. The key idea of the localization method is to exploit the relationship between micropipette resistance and tip-membrane distance, enabling vision-independent sensing of neuronal proximity. We establish this resistance-distance relationship through theoretical modeling and parameter identification using FEM. To ensure high resistance signal fidelity, we further develop a filtering algorithm to suppress measurement noise and extract clean resistance signals, from which the cell motion can be accurately inferred. The proposed method is experimentally validated on neurons from acute brain slices, where controlled periodic micropipette displacements are used to mimic physiological motion. The results show that the RMSE between the estimated proximity distance and the actual displacement amplitude is below 0.5 μm, confirming the high accuracy of the proposed sensing method. Based on this estimation, we design a phase-synchronized capture strategy that synchronizes the micropipette arrival with the cell's farthest position relative to the micropipette tip, ensuring optimal membrane contact. Experimental results in anesthetized mice show that the proposed strategy outperformed three baselines. Our strategy achieves a final average micropipette resistance of 1.34 GΩ, significantly higher than 24.38 ± 13.28 MΩ (NP), 112.98 ± 15.71 MΩ (AP), and 347.24 ± 58.76 MΩ (TP). Finally, we integrated the proposed resistance-based sensing method and phase-synchronized approach strategy into a widely used patch-clamp platform, enabling robotic in vivo patch-clamp recording. We successfully performed both whole-cell and cell-attached recordings with a seal formation success rate of 81.8%, notably higher than 51% and 24% achieved by previous autonomous systems. We further extend the same system to anesthetized rats and to marmosets under both anesthetized and awake conditions, obtaining cell-attached recordings. Notably, this work represents the first demonstration of robotic in vivo patch-clamp recordings in awake marmosets, demonstrating reliable performance across species and brain states.

Acknowledgements
This work was supported by the National Natural Science Foundation of China (Grant No. 62027812, 62273186); the Basic and Applied Basic Research Foundation of Guangdong Province (Grant No. 2024A1515011171); the Shenzhen Science and Technology Innovation Program (Grant No. JCYJ20250604185817023), and the Beijing Advanced Innovation Center for Intelligent Robots and Systems (Grant No. 2019IRS05). Zhao Qili gratefully acknowledges the support of the TCL Youth Scholarship.

Author details
[1]National Key Laboratory of Intelligent Tracking and Forecasting for Infectious Diseases, Engineering Research Center of Trusted Behavior Intelligence, Ministry of Education, Tianjin Key Laboratory of Intelligent Robotics, Institute of Robotics and Automatic Information System, Nankai University, Tianjin, China. [2]Institute of Intelligence Technology and Robotic Systems, Shenzhen Research Institute of Nankai University, Shenzhen, China. [3]Hong Kong Plexon Co. Ltd., Hong Kong, China. [4]Laboratory of Traditional Chinese Medicine Neuroscience, Shandong University of Traditional Chinese Medicine, Jinan, China. [5]Experimental Center, Shandong University of Traditional Chinese Medicine, Jinan, China. [6]Laboratory of Neurobiology, School of Basic Medical Sciences, Tianjin Medical University, Tianjin, China. [7]Beijing Advanced Innovation Center for Intelligent Robots and Systems, Beijing Institute of Technology, Beijing, China

Author contributions
Ruimin Li: Writing - original draft, Investigation, Formal analysis, Conceptualization. Hao Chen: Writing - review & editing, Investigation. Bo Hu: Writing - review & editing, Investigation. Jinyu Qiu: Writing - review & editing. Yuzhu Liu: Writing - review & editing. Zijian Guo: Conceptualization. Shouguo Wu: Conceptualization. Mengya Liu: Writing - review & editing. Ran Ding: Methodology. Shengkai Ding: Methodology. Yuanyuan Liu: Resources. Xiaogang Pang: Resources. Hui Shen: Resources. Qili Zhao: Supervision, Resources, Project administration, Funding acquisition, Conceptualization. Xin Zhao: Supervision, Resources, Project administration, Funding acquisition, Conceptualization.

Data availability
The data supporting the findings of this study are included in this published article and its supplementary information files. Additional datasets are available from the corresponding author upon reasonable request.

Conflict of interest
The authors declare no competing interests.

Ethics declarations
All animal procedures involving mice and rats were approved by the Experimental Animal Ethics Committee of Nankai University and were conducted in accordance with the relevant animal management regulations of the Ministry of Health of the People's Republic of China. All procedures involving marmosets were approved by the Experimental Animal Ethics Committee of Shandong University of Traditional Chinese Medicine and were performed in compliance with the corresponding institutional and national regulations.

Supplementary information The online version contains supplementary material available at https://doi.org/10.1038/s41378-026-01325-x.

Received: 23 January 2026 Revised: 6 March 2026 Accepted: 30 March 2026

References

1. Gao, J., Liao, C., Liu, S., Xia, T. & Jiang, G. Nanotechnology: new opportunities for the development of patch-clamps. *J. Nanobiotechnol* **19**, 97 (2021).
2. Jacques, R. et al. Photoelectrochemical imaging of single cardiomyocytes and monitoring of their action potentials through contact force manipulation of organoids. *Biosens Bioelectron* **223**, 115024 (2023).
3. Kawatani, M. & Yamashita, T. In vivo whole-cell recording from the mouse brain. *Methods Mol. Biol.* **2794**, 245–257 (2024).
4. Noguchi, A., Ikegaya, Y. & Matsumoto, N. In vivo whole-cell patch-clamp methods: recent technical progress and future perspectives. *Sensors* **21**, 1448 (2021).
5. Tao, C., Zhang, G., Xiong, Y. & Zhou, Y. Functional dissection of synaptic circuits: in vivo patch-clamp recording in neuroscience. *Front Neural Circuits* **9**, 23 (2015).
6. Amemori, S., Amemori, K.-I., Cantor, M. L. & Graybiel, A. M. A non-invasive head-holding device for chronic neural recordings in awake behaving monkeys. *J. Neurosci Methods* **240**, 154–160 (2015).
7. Shahbazi, E. et al. 3D-printable non-invasive head immobilization system for non-human primates. *J. Neurosci Methods* **425**, 110593 (2026).
8. Holst, G. L. et al. Autonomous patch-clamp robot for functional characterization of neurons in vivo: development and application to mouse visual cortex. *J. Neurophysiol* **121**, 2341–2357 (2019).
9. Sato, M. et al. Simultaneous monitoring of mouse respiratory and cardiac rates through a single precordial electrode. *J. Pharm Sci.* **137**, 177–186 (2018).
10. Fee, M. S. Active stabilization of electrodes for intracellular recording in awake behaving animals. *Neuron* **27**, 461–468 (2000).
11. Annecchino, L. A. et al. Robotic automation of in vivo two-photon targeted whole-cell patch-clamp electrophysiology. *Neuron* **95**, 1048–1055.e3 (2017).
12. Komai, S., Denk, W., Osten, P., Brecht, M. & Margrie, T. W. Two-photon targeted patching (TPTP) in vivo. *Nat. Protoc* **1**, 647–652 (2006).
13. Dembitskaya, Y. et al. Shadow imaging for panoptical visualization of brain tissue in vivo. *Nat. Commun* **14**, 6411 (2023).
14. Inavalli, V. V. G. K., Puente Muñoz, V., Draffin, J. E. & Tønnesen, J. Fluorescence microscopy shadow imaging for neuroscience. *Front Cell Neurosci* **18**, 1330100 (2024).
15. Suk, H.-J. et al. Closed-loop real-time imaging enables fully automated cell-targeted patch-clamp neural recording in vivo. *Neuron* **95**, 1037–1047.e11 (2017).
16. Fan, J. L. et al. High-speed volumetric two-photon fluorescence imaging of neurovascular dynamics. *Nat. Commun* **11**, 6020 (2020).
17. Stoy, W. M. et al. Compensation of physiological motion enables high-yield whole-cell recording in vivo. *J. Neurosci Methods* **348**, 109008 (2021).
18. Zhang, Y. et al. Physiological motion compensation for neuroscience research based on electrical bio-impedance sensing. *IEEE Sens J.* **23**, 25377–25389 (2023).
19. Furue H In Vivo Blind Patch-Clamp Recording Technique. In Patch Clamp Techniques (ed. Okada Y) 171–182 (Springer Japan, Tokyo, https://doi.org/10.1007/978-4-431-53993-3_11.
20. Margrie, T. W., Brecht, M. & Sakmann, B. In vivo, low-resistance, whole-cell recordings from neurons in the anaesthetized and awake mammalian brain. *Pflug Arch* **444**, 491–498 (2002).
21. Qiu, J. et al. Robotic fast patch clamp in brain slices based on stepwise micropipette navigation and gigaseal formation control. *Sensors* **25**, 1128 (2025).
22. Del Linz, S. et al. Contact-free scanning and imaging with the scanning ion conductance microscope. *Anal Chem* **86**, 2353–2360 (2014).
23. Rheinlaender, J. & Schäffer, T. E. An accurate model for the ion current-distance behavior in scanning ion conductance microscopy allows for calibration of pipet tip geometry and tip-sample distance. *Anal Chem* **89**, 11875–11880 (2017).
24. Hall, J. E. Access resistance of a small circular pore. *J. Gen Physiol* **66**, 531–532 (1975).
25. Newman, J. Resistance for flow of current to a disk. *J. Electrochem Soc.* **113**, 501–502 (1966).
26. Zhao, Q. et al. Robotic patch clamp based on noninvasive 3-D cell morphology measurement for higher success rate. *IEEE Trans Instrum Meas* **71**, 1–12 (2022).

27. Sánchez, D. et al. Noncontact measurement of the local mechanical properties of living cells using pressure applied via a pipette. *Biophys J.* **95**, 3017–3027 (2008).
28. Lu, Y.-B. et al. Viscoelastic properties of individual glial cells and neurons in the CNS. *Proc. Natl. Acad. Sci. USA.* **103**, 17759–17764 (2006).
29. VitalEar: An Earable Heartbeat and Respiratory Rate Monitoring System Under Aerobic Exercises | IEEE J Mag | IEEE Xplore. https://ieeexplore.ieee.org/document/11107319.
30. Perkins, K. L. Cell-attached voltage-clamp and current-clamp recording and stimulation techniques in brain slices. *J. Neurosci Methods* **154**, 1–18 (2006).
31. Do, T. L. et al. Interaction of SARS-CoV-2 Spike protein with ACE2 induces cortical actin modulation, including dephosphorylation of ERM proteins and reduction of cortical stiffness. *Hum Cell* **38**, 3 (2024).
32. Oral, I., Guzel, H. & Ahmetli, G. Measuring the Young's modulus of polystyrene-based composites by tensile test and pulse-echo method. *Polym Bull* **67**, 1893–1906 (2011).
33. Zhou, Y., Zhang, Q., Wang, H., Zhou, P. & Chai, T. EKF-based enhanced performance controller design for nonlinear stochastic systems. *IEEE Trans Autom Control* **63**, 1155–1162 (2018).
34. Guo Z et al. (2024) A robotic blind patch-clamp system based on cranial opening localization and micropipette guidance. In 2024 IEEE International Conference on Robotics and Biomimetics (ROBIO) 571–576. https://doi.org/10.1109/ROBIO64047.2024.10907311.
35. Kodandaramaiah, S. B., Franzesi, G. T., Chow, B. Y. & Boyden, E. S. Automated whole-cell patch-clamp electrophysiology of neurons in vivo. *Nat. Methods* **9**, 585–587 (2012).
36. Whole-Cell Recording In Vivo - R. DeWeese - 2007 - Current Protocols in Neuroscience - Wiley Online Library. https://currentprotocols.onlinelibrary.wiley.com/doi/abs/10.1002/0471142301.ns0622s38.
37. Desai, N. S., Siegel, J. J., Taylor, W., Chitwood, R. A. & Johnston, D. MATLAB-based automated patch-clamp system for awake behaving mice. *J Neurophysiol* **114**, 1331–1345 (2015).
38. Assembly and operation of the autopatcher for automated intracellular neural recording in vivo | Nature Protocols. https://www.nature.com/articles/nprot.2016.007.
39. Paukert, M. & Bergles, D. E. Reduction of motion artifacts during in vivo two-photon imaging of brain through heartbeat triggered scanning. *J Physiol* **590**, 2955–2963 (2012).
40. Al Ghamdi, K. S., Polgár, E. & Todd, A. J. Soma size distinguishes projection neurons from neurokinin 1 receptor-expressing interneurons in lamina I of the rat lumbar spinal dorsal horn. *Neuroscience* **164**, 1794–1804 (2009).
41. Shakoor, A., Gao, W., Zhao, L., Jiang, Z. & Sun, D. Advanced tools and methods for single-cell surgery. *Microsyst Nanoeng* **8**, 47 (2022).